The Astrophysical Journal, 978:51 (31pp), 2025 January 01 https://doi.org/10.3847/1538-4357/ad93b5

Analysis of Gamma-Ray Burst Closure Relationship in Multiple Wavelengths

M. G. Dainotti[1,2,3], S. Bhardwaj[1,2], E. Bissaldi[4,5], N. Fraija[6], S. Sourav[7], and A. Galvan-Gamez[6]
[1] National Astronomical Observatory of Japan, 2 Chome-21-1 Osawa, Mitaka, Tokyo 181-8588, Japan
[2] Department of Astronomical Sciences, The Graduate University for Advanced Studies, SOKENDAI, Shonankokusaimura, Hayama, Miura District, Kanagawa 240-0193, Japan
[3] Space Science Institute, 4765 Walnut Street Ste B, Boulder, CO 80301, USA
[4] Dipartimento Interateneo di Fisica "M. Merlin," Politecnico di Bari, Via E. Orabona 4, 70125 Bari, Italy
[5] Istituto Nazionale di Fisica Nucleare—Sezione di Bari, Via E. Orabona 4, 70125 Bari, Italy
[6] Instituto de Astronomía, Universidad Nacional Autónoma de México Circuito Exterior, C.U., A. Postal 70-264, 04510 México D.F., Mexico
[7] Department of Physics, Washington University in St. Louis, MO 63130, USA
Received 2024 February 06; revised 2024 October 28; accepted 2024 November 15; published 2024 December 24

Abstract

Gamma-ray bursts (GRBs) are intense pulses of high-energy emission associated with the death of massive stars or compact objects' coalescence. Their multiwavelength observations help verify the reliability of the standard fireball model. We analyze 14 GRBs observed contemporaneously in gamma rays by the Fermi Large Area Telescope, in X-rays by the Swift Telescope, and in the optical bands by Swift and many ground-based telescopes. We study the correlation between the spectral and temporal indices using closure relations according to the synchrotron forward-shock model in a stratified medium ($n \propto r^{-k}$) with k ranging from 0 to 2.5. We find that the model without energy injection is preferred over the one with energy injection in all the investigated wavelengths. In gamma rays, we only explored the $\nu > \max\{\nu_c, \nu_m\}$ (slow cooling, SC/fast cooling, FC) cooling condition (where ν_c and ν_m are the cooling and characteristic frequencies, namely the frequencies at the spectral break). In the X-ray and optical bands, we explored all the cooling conditions, including $\nu_m < \nu < \nu_c$ (SC), $\nu_c < \nu < \nu_m$ (FC), and SC/FC, and found a clear preference for SC for X-rays and SC/FC for optical. Within these cooling conditions, X-rays exhibit the highest rate of occurrence for the density profile with $k = 0$, while the optical band has the highest occurrence for $k = 2.5$ when considering no energy injection. Although we can pinpoint a definite environment for some GRBs, we find degeneracies in other GRBs.

Unified Astronomy Thesaurus concepts: Gamma-ray bursts (629)

1. Introduction

Gamma-ray bursts (GRBs) are immensely energetic transient events emitting radiation spanning the electromagnetic spectrum, from gamma rays down to X-rays, optical and radio, and up to TeV energies. They are conventionally categorized as short (SGRBs) and long (LGRBs), according to T_{90} duration. T_{90} is the time in which 90% of the counts, including the subtracted background, are emitted, between 5% and 95% of the total prompt emission as measured in the 50–300 keV band. LGRBs have $T_{90} > 2$ s, while SGRBs have $T_{90} < 2$ s (C. Kouveliotou et al. 1993).

The prompt emission is typically observed at high energies, from gamma rays to hard and soft X-rays, and sometimes also optical (see B. Zhang 2014, 2018, for a review). After the prompt emission, long-lasting emission known as afterglow can typically be observed in soft X-rays, optical, and radio bands (see P. Kumar & B. Zhang 2015; B. Zhang 2018, for reviews). The afterglow emission is sometimes detected at high energies, too, in the MeV–GeV–TeV energy range. GRB 090510 is one of the earliest examples where such behavior was observed (M. Ackermann et al. 2010).

Swift X-ray light curves (LCs) have demonstrated that these LCs display complex characteristics beyond a simple power law. These characteristics have been thoroughly investigated by G. Tagliaferri et al. (2005), B. Zhang et al. (2006), J. A. Nousek et al. (2006), P. T. O'Brien et al. (2006), B. Zhang et al. (2007b, 2007a), B.-B. Zhang et al. (2007), B. Zhang (2007a), T. Sakamoto et al. (2007), L. Zhao et al. (2019), and N. Fraija et al. (2019). A notable characteristic identified in LCs is the presence of a plateau, which refers to a period of relatively constant luminosity that follows the prompt emission of GRBs and comes before the subsequent decay of the afterglow. The occurrence of plateaus has been observed in different wavelengths, such as X-ray (J. A. Nousek et al. 2006; P. T. O'Brien et al. 2006; B. Zhang et al. 2006; T. Sakamoto et al. 2007; P. A. Evans et al. 2009), optical (M. G. Dainotti et al. 2020b, 2022c), and radio (D. Levine et al. 2022). These plateaus typically last between 10^2 and 10^5 s and tend to be attributed to a central engine supplying energy for a long time (Z. G. Dai & T. Lu 1998; M. J. Rees & P. Mészáros 1998; R. Sari & P. Mészáros 2000; B. Zhang & P. Mészáros 2001; B. Zhang et al. 2006; B. Zhang 2007a; E.-W. Liang et al. 2007, 2008; B. Zhang 2011). This injection of energy can occur through mechanisms such as the fallback of accreting matter onto a black hole (P. Kumar et al. 2008; J. K. Cannizzo & N. Gehrels 2009; J. K. Cannizzo et al. 2011; P. Beniamini et al. 2017; L. Li et al. 2018b; B. D. Metzger et al. 2018) or the spin-down luminosity from a newborn magnetar (B. Zhang & P. Mészáros 2001; E. Troja et al. 2007; K. Toma et al. 2007; A. Rowlinson et al. 2010; S. Dall'Osso et al. 2011; B. P. Gompertz et al. 2013; A. Rowlinson et al. 2013; B. P. Gompertz et al. 2014; H.-J. Lü & B. Zhang 2014; A. Rowlinson et al. 2014; B. P. Gompertz et al. 2015; H.-J. Lü et al. 2015; N. Rea et al. 2015; P. Beniamini & R. Mochkovitch 2017; L. Li et al. 2018b; B. D. Metzger et al. 2018; G. Stratta

et al. 2018; N. Fraija et al. 2021). Another significant feature often observed in GRB afterglow LCs is the presence of an achromatic break, commonly referred to as jet break, which indicates that GRB jets are highly collimated. A subsequent steep decline is observed in the LC following this jet break. This decline happens because the jet decelerates as it interacts with the surrounding ambient medium, and its emission becomes less beamed. This steepening of the LC is driven by two primary factors: the relativistic beaming of the emission, and the lateral expansion of the jet as it spreads out and widens (J. E. Rhoads 1999; R. Sari et al. 1999; P. Kumar & B. Zhang 2015).

The standard fireball model has become widely accepted as one of the most reliable models for describing both the prompt emission and the long-lasting afterglow of GRBs (R. Sari & T. Piran 1995; R. Sari et al. 1996; R. Sari & T. Piran 1999; P. Kumar & T. Piran 2000; J. Granot & R. Sari 2002; B. Zhang & P. Mészáros 2004; B. Zhang et al. 2006). The long-lasting afterglow emission can be explained by this model through its association with the interplay between the relativistic outflow and the external medium in its vicinity (R. Sari & T. Piran 1999; P. Kumar & T. Piran 2000). An essential component of the conventional fireball model involves the interaction of the shells of the expanding plasma with the external medium. This interaction generates a so-called external forward shock (FS). A quick test of the standard fireball model can be verified using closure relations (CRs; see H. Gao et al. 2013, for a review). CRs are described by the equations that establish the relationships between the spectral index, denoted as β, and the temporal index, denoted as α, of a given segment of the LC. The α and β parameters are related to the flux according to the convention $F_\nu \propto t^{-\alpha}\nu^{-\beta}$. In an external FS, electrons primarily undergo acceleration and cooling through synchrotron radiation. The formulation of the CR equations relies on specific assumptions concerning the hypothetical astrophysical environment. These assumptions encompass scenarios such as a uniform-density interstellar medium (ISM) and stellar wind environment, as well as a stratified medium due to plasma instabilities that adhere to a power-law relationship, denoted as $n(r) \propto r^{-k}$, where k falls within the range 0–2.9 (P. Kumar & T. Piran 2000; P. A. Crowther 2007; F. De Colle et al. 2012a, 2012b; H. Gao et al. 2013; S.-X. Yi et al. 2013; N. Fraija et al. 2020a; S.-X. Yi et al. 2020; M. Dainotti et al. 2023).

Most studies of CRs have focused on investigating the environments that correspond to the ISM and stellar wind, characterized by values of $k = 0$ and $k = 2$, respectively (A. Panaitescu & P. Kumar 2000; R. A. Chevalier & Z. Li 2000; E. Ramirez-Ruiz et al. 2001, 2005; M. Dainotti et al. 2023). The inclusion of the wind medium is typically associated with the stellar wind the massive star emits before its collapse. The presence of a stratified medium is crucial in understanding the evolution of the relativistic blast wave generated by GRBs. As the relativistic ejecta from the GRB interacts with the surrounding medium, the blast wave undergoes a transition between different phases of this evolution, from being relativistic to nonrelativistic (F. De Colle et al. 2012a). The stratified medium serves as a key factor in this transition between the relativistic phase, governed by the Blandford–McKee self-similar solution, and the subsequent Newtonian phase described by the Sedov–Taylor solution (F. De Colle et al. 2012a).

Previous research has been conducted in separated wavelengths in high-energy gamma rays, X-rays, and optical.

1.1. Previous Studies on the Closure Relations in Gamma Rays

Temporally prolonged emission at high energies, typically lasting for hundreds to thousands of seconds and occurring at energies $\geqslant$100 MeV, is often explained using the synchrotron FS model. Consequently, this high-energy emission is expected to conform to the CRs associated with the synchrotron FS model (P. Kumar & R. B. Duran 2009, 2010). The Large Area Telescope (LAT) instrument on board the Fermi Gamma-ray Space Telescope (Fermi-LAT; W. B. Atwood et al. 2009) plays a crucial role in detecting and measuring these high-energy GRBs ranging from 20 MeV to over 300 GeV. The work of D. Tak et al. (2019), M. G. Dainotti et al. (2021b), and M. Dainotti et al. (2023) has delved into CRs within the realm of gamma rays. D. Tak et al. (2019) analyzed 59 GRBs taken from Fermi-LAT. They selected these GRBs based on stringent criteria, requiring the uncertainty on their temporal indices and spectral indices to be less than one-half and one-third, respectively. Their analysis revealed that while the standard synchrotron FS emission model effectively characterizes the spectral and temporal indices for most cases, a substantial fraction of GRBs could not be adequately characterized within this framework. Among their key findings, they also discovered that GRBs which fail to conform to any CRs have a temporal decay index $\alpha_{\rm LAT} < 1$, indicative of a relatively gradual decay. There are a few cases in which the plateau emission has been discovered also at high energies (M. Ajello et al. 2019). M. G. Dainotti et al. (2021b) examined CRs for three specific GRBs (090510A, 090902B, and 160509A). The study determined that this set of GRBs conformed to a slow-cooling (SC) environment ($\nu_m < \nu_{\rm LAT} < \nu_c$) rather than a fast-cooling (FC) environment ($\nu_c < \nu_{\rm LAT} < \nu_m$), where ν_m and ν_c are the characteristic and cooling frequencies at the spectral break, regardless of whether they were situated in a constant-density ISM or a stellar wind medium (see R. Sari et al. 1998).[8] On the other hand, the analysis performed by M. Dainotti et al. (2023) differs from that done by D. Tak et al. (2019), as they used a bigger sample (86 versus 59 in D. Tak et al. 2019) and focused on CRs with both broken power-law (BPL) and simple power-law (PL) fitting, not only PL fitting, as done by D. Tak et al. (2019). Furthermore, M. Dainotti et al. (2023) employed a frequentist approach to classify the fulfillment of CRs rather than the Bayesian probability performed by D. Tak et al. (2019). However, they also found similar results, with most of the GRBs in their sample fulfilling the CRs in the SC regime either in a constant-density ISM or stellar wind environment. M. Dainotti et al. (2023) found that out of 86 GRBs in their sample, taken from the Fermi-LAT Second Gamma-ray Burst Catalog (2FLGC; M. Ajello et al. 2019), 74 of them comply with at least one CR, indicating that many of the features observed in high-energy GRBs can be explained by the external FS model. Thus, 12 GRBs from their sample do not fulfill any CRs, which is of interest for the current study. After summing the contribution of the fulfillment rates in each case, they observed a preference for CRs without energy injection over those assuming energy injection. They found that for CRs without energy injection, 35 GRBs satisfy at least one CR.

[8] Where the timescale of cooling for shocked electrons is of the same order or longer than the GRB jet's dynamic timescale.

They also considered a subsample of the 21 GRBs fitted with a BPL and found that eight GRBs (090926A, 091003, 110731A, 130504C, 160509A, 160816A, 171010A, and 171120A) have α and β parameters in alignment with the $\nu > \max\{\nu_c, \nu_m\}$ regime for all values of k. However, in the case of CRs with energy injection, they found 15 GRBs that failed to adhere to any of the CRs. They also performed Markov Chain Monte Carlo simulations, which indeed support these conclusions.

N. Fraija et al. (2024b) derived the CRs in a stratified medium with variations of microphysical parameters of the synchrotron and synchrotron self-Compton (SSC) FS model (for the introduction of the thermal component, refer to D. C. Warren et al. 2022). In the analytical investigation of previous works (T. Fukushima et al. 2017), it has been shown that even if the emission mechanism is switching from synchrotron to SSC, the gamma-ray LCs can be a smooth PL, which agrees with the observed LCs in GeV emission.

Furthermore, N. Fraija et al. (2023b) estimated the CRs in an off-axis FS scenario to investigate the spectral and temporal index evolution of the bursts reported in the 2FLGC. Finally, N. Fraija et al. (2024a) introduced the SSC reverse-shock (RS) scenario in a stratified environment for the thick- and thin-shell regimes, and showed that this emission can reproduce the early LCs exhibited in some bursts reported in the 2FLGC.

Since a significant fraction of the afterglow phase in GeV emission in the Fermi-LAT data cannot be explained by CRs using the standard fireball synchrotron FS model, N. Fraija et al. (2020b) proposed the possibility of a significant contribution from the SSC process (P. Veres & P. Mészáros 2014; D. C. Warren et al. 2022). To this end, N. Fraija et al. (2022a) studied the CRs for Fermi-LAT GRBs in the SSC afterglow model context using the 2FLGC, and found they could explain a considerable portion of bursts with a constant or stellar wind medium. A recent study by N. Fraija et al. (2023a) examined the CRs for Fermi-LAT GRBs in the framework of the SSC afterglow model also accounting for an intermediate-density profile ($\propto r^{-k}$) with $0 \leqslant k \leqslant 2.5$, which considers several scenarios, including the adiabatic/radiative regime and the presence or absence of energy injection. They investigated these aspects for all possible values of the electron spectral index, p. The study's findings revealed that the afterglow SSC model with an intermediate-density profile successfully explains a significant subset of GRBs that do not follow the stellar wind or constant medium environment.

1.2. Previous Studies on the Closure Relations in X-Rays

In the X-rays regime, J. L. Racusin et al. (2009), G. P. Srinivasaragavan et al. (2020), and M. G. Dainotti et al. (2021a) performed studies for CRs. Their analysis showed that most GRBs within their sample can be ascribed to the external FS model, as predicted by the standard fireball model. These models do not assume a structured jet as G. Ryan et al. (2020). The most preferred scenario is the SC regime, regardless of a constant or a stellar medium environment. J. L. Racusin et al. (2009) explored the CRs for both the ISM and stellar wind environments, considering cases with and without energy injection. G. P. Srinivasaragavan et al. (2020) fitted 455 X-ray LCs that exhibit the plateau phase. They investigated whether these LCs follow the CRs in two different astrophysical environments and cooling regimes within the external FS model. They found that the most favored environments in the SC regime are a wind medium or a constant-density ISM. They also confirmed the existence of the 3D fundamental plane relation (also known as the Dainotti relation) between the rest-frame time and luminosity at the end of the plateau emission and the peak prompt luminosity, with a much larger sample compared to previous studies (for more on the 3D fundamental plane relation, see M. G. Dainotti et al. 2016; M. G. Dainotti et al. 2020a; M. G. Dainotti et al. 2022c). They further segregated the sample of GRBs following the Dainotti relation within groups corresponding to distinct astrophysical environments found by studying the CRs. This plane emerges as a model discriminator for these environments. The metrics used to determine if a given environment and energy emission mechanism can be promoted as possible standard candles are obtained by looking at the best-fit parameters and their dispersions. The smaller the dispersion of the fundamental plane, the better the sample is considered a standard candle. They found that the sample of GRBs which have peculiar CRs exhibit an intrinsic scatter σ that is compatible within a 1σ range of the "Gold" GRBs, a subset of LGRBs featuring relatively flat plateaus. Although this analysis has not led to a smaller dispersion for these samples, it is still a pathway to lead to standard candle samples comparable to the golden sample dispersion. M. G. Dainotti et al. (2021a) also analyzed 455 X-ray LCs to examine these GRBs' emission mechanisms and astrophysical environments by studying CRs within the time interval of the plateau emission. They found that the most recurrent environments for the electron spectral distribution, $p > 2$, are wind SC and ISM SC for cases where the parameter q, indicating the flatness of the plateau emission and incorporating energy injection, is 0 and 0.5, respectively. They also find that, for SGRBs, all ISM environments with $q = 0$ have the smallest $\sigma = 0.04 \pm 0.15$ in terms of the fundamental plane relation. They have shown that most GRBs presenting plateau emission fulfill the CRs, including the energy injection, with a particular preference for the wind SC environment. Again, similarly to the study of the post-plateau phase, in this case GRBs which fulfill the given relations can be used as possible standard candles. Moreover, these findings offer insights into possible strategies for diminishing the intrinsic scatter observed in these investigated relationships (M. G. Dainotti et al. 2017a, 2022b).

1.3. Previous Studies on the Closure Relations in the Optical Domain

In the optical domain, a previous study by S. R. Oates et al. (2012) examined 48 GRBs observed by Swift. Their analysis indicated that almost half of the GRBs in their sample conformed to the standard fireball model determined by the CRs. They evaluated CRs in three different density profiles: one for a wind-like density environment, one for a constant-density ISM environment, and one independent of the density profile of the external medium, i.e., $\nu_{\rm opt} > \nu_c$. In the first scenario, six GRBs follow a constant medium; in the second scenario, seven GRBs follow the wind medium; and eight GRBs follow the third scenario. M. Jelínek et al. (2022) investigated the optical afterglow of LGRB 190919B and concluded that it follows the CR for a SC regime with constant ISM. Recently, M. G. Dainotti et al. (2022a) studied CRs in the optical band using a sample of 82 GRBs. Their study found that the most favored regime is $\nu > \max\{\nu_c, \nu_m\}$ for both the ISM and stellar wind medium. Similarly to what has been done in X-rays, they tested the 2D Dainotti correlation between the rest-frame end time of the plateau and the luminosity at that time (M. G. Dainotti et al. 2008, 2010, 2011, 2013; M. Dainotti et al. 2015; R. Del Vecchio et al. 2016; M. G. Dainotti et al.

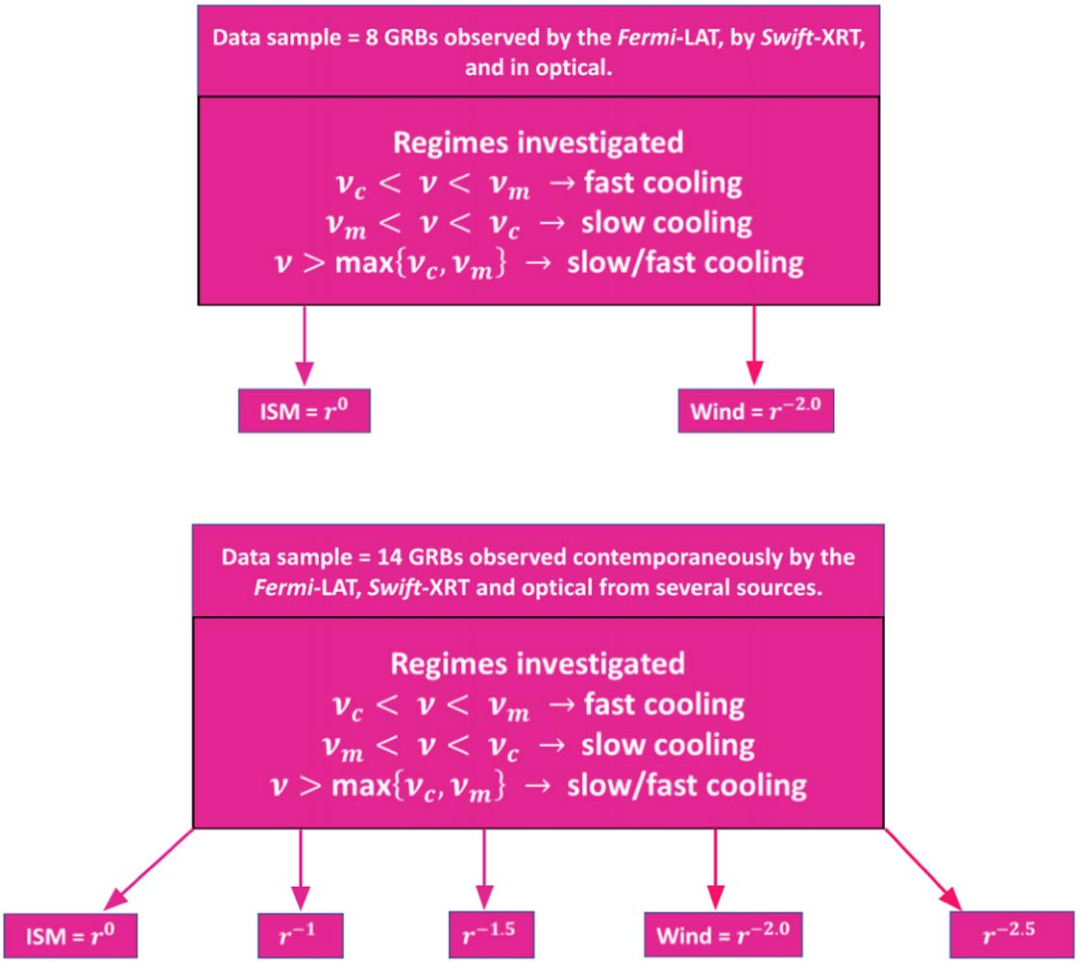

Figure 1. Top: illustration depicting the GRB sample and regimes explored in prior multiwavelength studies. Bottom: schematic of the GRB sample and regimes investigated in this study in the multiwavelength domain.

2017b, 2020b, 2022c) for GRBs which satisfy the favored CRs, to understand if these samples are better suited for cosmological analysis and have a physical grounding in the framework of the standard fireball model. They found that the scatter within this sample in the 2D Dainotti relation is compatible with the previous values in the X-ray (M. G. Dainotti et al. 2013; G. P. Srinivasaragavan et al. 2020; M. G. Dainotti et al. 2021a), optical (M. G. Dainotti et al. 2020b, 2022c), and radio (D. Levine et al. 2022), within the 1σ range, both before and after correcting for selection biases. Like X-rays, this method identifies subsets of GRBs underlying a physical emission mechanism or a peculiar environment that could pave the way for using GRBs as standard candles.

1.4. Previous Study of Closure Relations in Multiple Wavelengths

The following studies in this section investigated what fraction of GRBs satisfied the CRs within the standard fireball model in order to determine the favored environment and energy mechanism. The top panel of Figure 1 summarizes the GRB sample and regimes explored of previous studies conducted in the multiwavelength domain.

P. Afonso et al. (2011) analyzed GRB 050502B to examine the possible correlation between its X-ray and optical data. They found that GRB 050502B follows the CR in the fireball synchrotron FS model for both a constant-density ISM and stellar wind medium. M. Ackermann et al. (2013) and X.-G. Wang et al. (2015) examined CRs in both X-rays and optical wavelengths. M. Ackermann et al. (2013) analyzed CRs involving X-ray and optical data for GRB 110731A, which had also been observed by Fermi-LAT. They found that GRB 110732A favored the SC regime in a stellar wind environment. X.-G. Wang et al. (2015) conducted a comprehensive study involving 85 GRBs observed by Swift. Their analysis also focused on testing the CRs in the X-ray and optical, aiming to test their consistency with the synchrotron FS model. Within their sample, they identified 45 out of 85 GRBs that exhibited an achromatic break, and these GRBs were found to align with the standard CRs of the external FS model across all segments of their afterglows. Furthermore, their study identified an additional 37 GRBs that did not entirely satisfy the CRs in one or more segments of their afterglows but did display an achromatic break. This suggests that the synchrotron FS model could partially describe a substantial portion of their sample, even though there were deviations in some regions of their afterglow LCs. In the study of T. Fukushima et al. (2017), numerical models were employed to simulate X-ray and optical LCs within an ISM environment, accounting for both FC and SC regimes. They applied these simulation models specifically to the case of GRB 130427A, and found that a more complex and refined model is required to describe the behavior of this burst. B. P. Gompertz et al. (2018) analyzed a sample of 56

LGRBs detected by Fermi-LAT/Gamma-ray Burst Monitor (GBM) in gamma rays and by the Swift X-ray Telescope (XRT) as well as optical and NIR telescopes by performing a fitting of the temporal and spectral indices of these GRBs using the synchrotron CRs. We note that, between our study and this one, we have seven GRBs in common, though our study includes 230,812, so it includes new data for more than 8 yr. The difference is that we restrict ourselves to the Fermi-LAT data. Another key difference is that they focused on two density profiles (wind medium and ISM), while we also explore a stratified medium (r^{-1}, $r^{-1.5}$, and $r^{-2.5}$) along with the wind and ISM environments, providing a comprehensive analysis of the CRs to test the external synchrotron FS model.

A recent study conducted by T. Kangas & A. S. Fruchter (2021) provides a comparative analysis of the observed patterns in radio LCs and their counterparts in the X-ray and optical domains. They used a sample of 21 GRBs with radio LCs in their afterglow phase. Their findings indicated a substantial incompatibility between radio LCs and the observed patterns exhibited by X-ray and optical LCs. They concluded that the radio LCs are inconsistent with the standard fireball model. Similarly, K. Misra et al. (2021) investigated the afterglow of GRB 190114C across several wavelengths, encompassing X-ray, optical, and radio observations. Their analysis revealed that the X-ray and radio LCs exhibited behaviors inconsistent with predictions based on the standard fireball model for GRB afterglows.

A recent detailed study by H. Dereli-Begue et al. (2022) was conducted on a sample comprising 13 GRBs exhibiting well-defined X-ray plateaus along with optical counterparts. The study identified three distinct phases within the LCs of these GRBs: first, the plateau phase; second, the transition from the plateau to a decaying LC (marking the first break as the end of the plateau); and, third, a second, late-time break, called a jet break, which typically occurs when the relativistic jet begins to decelerate significantly. They explored two cooling regimes, namely fast ($\nu_m > \nu_c$) and slow ($\nu_c > \nu_m$), each of them divided into three regions. For FC, the regions are defined as A ($\nu < \nu_c < \nu_m$), B ($\nu_c < \nu < \nu_m$), and C ($\nu_c < \nu_m < \nu$). For SC, the regions are defined as D ($\nu < \nu_m < \nu_c$), E ($\nu_m < \nu < \nu_c$), and F ($\nu_m < \nu_c < \nu$). Their study primarily focused on regions C, E, and F, demonstrating that the CRs are independently satisfied within each wavelength band and during each phase of the LC.

In this work, we present the first comprehensive analysis and evaluation of CRs using multiwavelength observations in the context of the synchrotron FS model for a combined sample observed in gamma rays, X-rays, and optical wavelengths. We aim to understand the validity of the standard fireball model. The main idea is to conduct a comprehensive analysis by comparing individual GRBs, employing a novel approach. A deeper understanding of GRBs' fundamental characteristics can be achieved by examining CRs across multiple wavelengths. This could advance our ability to categorize and standardize GRBs for cosmological studies in forthcoming studies.

The bottom panel of Figure 1 shows an overview of our study. The paper is structured as follows. Section 2 provides a description of the data sample used in our analysis. In Section 3, we show the initial data analysis, which requires fitting the LCs, a necessary step for evaluating the CRs. In that section, we also present the methodology used to examine the theoretical CRs associated with constant ISM, stellar wind, and stratified environments. Finally, Section 4 provides a detailed summary of our results and conclusions.

2. Data Sample

The sample used in this study comprises 14 GRBs contemporaneously observed in gamma rays, X-rays, and optical wavelengths. To obtain our final sample of 14 GRBs for our analysis, we initially took 33 GRBs from Fermi-LAT, observed from 2008 August 18 to 2023 August 12, each with measured redshift. This group includes the brightest of all time (or so-called BOAT) GRB (221009A), and since the Fermi-LAT data for this GRB is not yet public, it was excluded from our analysis. Thus, we are left with 32 GRBs from Fermi-LAT, each with measured redshift, temporal indices (α), and spectral indices (β). We further excluded three GRBs due to their high relative errors ($\delta\alpha_{\rm LAT}/\alpha_{\rm LAT} > 1$ and $\delta\beta_{\rm LAT}/\beta_{\rm LAT} > 1$), resulting in a sample of 29 GRBs. The Fermi-LAT data were taken from the official Fermi-LAT analysis presented in the 2FLGC (M. Ajello et al. 2019).[9]

In the same period as the Fermi-LAT observations, 349 GRBs with measured redshifts were documented in the optical catalog (see M. G. Dainotti et al. 2024). Of these, 27 GRBs overlapped with our Fermi-LAT sample. Within this subset, 17 GRBs had documented $\beta_{\rm opt}$ from the literature and satisfied the criterion $\delta\beta_{\rm opt}/\beta_{\rm opt} < 1$. From these, we selected 16 GRBs with redshift information obtained from spectroscopy rather than photometry. One GRB was excluded because it only had two data points from Swift-XRT, resulting in a sample of 15 GRBs. We then conducted color evolution analysis on the optical data of these 15 GRBs (see Section 3) and excluded another GRB that had only two data points in the optical spectrum after the color evolution analysis. This process yielded a final data sample of 14 GRBs. The XRT data were taken from the Swift-BAT+XRT repository (P. A. Evans et al. 2009),[10] while the optical data for all the 14 GRBs were taken from M. G. Dainotti et al. (2024). More precisely, the optical data were gathered from Swift-UVOT (P. W. A. Roming et al. 2005) and 416 ground-based telescopes, as outlined in M. G. Dainotti et al. (2022c). The complete list of our sample of 14 GRBs is given in Tables 1, 2, and 4. All the temporal and spectral fits are tabulated with their corresponding uncertainties. When a model does not provide a reliable fit, it is replaced by a "…" in all tables. In Table 1, we also provide the T_{90} and $E_{\rm iso}$ for each GRB in our sample. Figure 2 shows the distribution of $\log E_{\rm iso}$ versus $\log \log T^*_{90}$ for the bursts in our sample (large red dots), together with all other GRBs with redshifts reported in the Fermi-GBM catalog (gray dots). Quantities marked with "*" refer to rest-frame-calculated values. In Figure 2, there is a positive correlation, with a Pearson coefficient of 0.52, which aligns with previous analyses in the literature. M. Dainotti et al. (2015) showed a positive correlation between the energy released during the prompt episode versus the time of the pulses, which on average roughly corresponds to the T^*_{90}. There is no particular clustering of the data in any region of the $\log E_{\rm iso}$ versus $\log T^*_{90}$ distribution, but the data tend to be on the higher end of the $E_{\rm iso}$ distribution.

We here stress that the optical spectral indices have been taken from various sources in the literature, which are quoted in the seventh column of Table 4, and that we consider only the GRBs for which we have not found color evolution. For a more detailed analysis of how we determine the color evolution, refer to Section 3.

[9] https://www-glast.stanford.edu/pub_data/953/2FLGC/
[10] https://www.swift.ac.uk/xrt_live_cat/

Table 1
Best-fit Parameters of the Temporal and Spectral Indexes from the Gamma-Ray Analysis

GRB Name	Gamma-Ray LC Best-fit Model	T_{90} (s)	$E_{\rm iso}$ ($\times 10^{52}$ erg)	$\alpha_{\gamma_1} \pm \delta_{\alpha_{\gamma_1}}$	$\alpha_{\gamma_2} \pm \delta_{\alpha_{\gamma_2}}$	$\beta_\gamma \pm \delta_{\beta_{\gamma_{\rm err}}}$	$\log(t_{\rm start})$ (s)	$\log(t_{\rm end})$ (s)	$\log(t_{\rm break})$ (s)	$\log(t_{\rm start,EI})$ (s)	$\log(t_{\rm end,EI})$ (s)	$\log(t_{\rm plateau})$ (s)
090328A	BPL	61.7 ± 1.8	2.7 ± 0.4	0.73 ± 0.43	1.06 ± 0.14	1.20 ± 0.13	1.32	5.00	2.40	1.32	2.40	2.36
090510A	BPL	0.96 ± 0.14	5.8 ± 0.5	2.32 ± 0.18	1.34 ± 0.18	1.05 ± 0.06	−0.17	4.96	0.60	−0.17	0.60	3.3
090902B	BPL	19.3 ± 0.3	47 ± 2	1.87 ± 0.17	1.24 ± 0.23	0.94 ± 0.04	0.35	4.99	2.20	0.35	2.20	2.20
090926A	BPL	13.8 ± 0.3	149 ± 8	1.77 ± 0.17	1.10 ± 0.17	1.14 ± 0.05	0.60	4.98	2.00	0.60	2.00	1.98
120711A	PL	44.0 ± 0.7	10 ± 2	…	1.63 ± 0.24	1.06 ± 0.17	2.65	4.96	…	2.65	4.96	4.96
130427A	BPL	138 ± 3	8.6 ± 0.4	0.79 ± 0.16	1.42 ± 0.10	0.99 ± 0.04	0.26	4.96	2.70	0.26	2.70	2.70
141028A	PL	31.49 ± 2.4	9 ± 2	…	0.97 ± 0.03	1.44 ± 0.23	1.15	4.98	…	1.15	4.98	4.98
160625B	PL	453.4 ± 0.6	17 ± 1	…	2.24 ± 0.28	1.35 ± 0.07	1.93	4.99	…	1.93	4.99	4.99
170405A	PL	78.6 ± 0.6	16 ± 7	…	1.27 ± 0.01	1.79 ± 0.35	1.54	4.98	…	1.54	4.98	4.98
171010A	BPL	107.3 ± 0.8	0.21 ± 0.03	2.24 ± 0.73	0.97 ± 0.29	1.04 ± 0.13	2.58	4.99	2.90	2.58	2.90	2.61
180720B	BPL	48.9 ± 0.4	2.2 ± 0.2	1.46 ± 0.19	3.20 ± 0.56	1.23 ± 0.10	1.22	4.99	2.37	1.22	2.37	2.34
210822A	PL	180 ± 40[c]	95 ± 8[d]	…	0.57 ± 0.18	1.11 ± 0.36	2.99	4.97	…	2.99	4.97	4.98
220101A	PL	128 ± 16	364 ± 23[e]	…	1.10 ± 0.53	1.54 ± 0.25	1.62	4.99	…	1.62	4.99	4.99
230812B	PL	3.3 ± 0.1	12 ± 1[f]	…	1.14 ± 0.07	1.16 ± 0.14	−0.74	4.54	…	−0.74	4.54	4.54

Notes. Columns (1) and (2): GRB names and the best-fit models, respectively. Columns (3) and (4): T_{90} (in the 50–300 keV energy range)[a] and $E_{\rm iso}^{\rm b}$ for each GRB, respectively. Columns (5) and (6): first temporal slope of the BPL fit (α_{γ_1}) and the second temporal slope of the BPL fit (α_{γ_2}), respectively; when the BPL is not a viable model for the paucity of data points, we adopt the PL model. Column (7): the spectral parameter, β_γ, which is the same in the two segments of the LC. Columns (8) and (9): start and end times of the LC, respectively. Column (10): break time between the two segments of the BPL. Columns (10) and (11): start and end times of the energy injection. Column (12): duration of the plateau.

[a] From https://heasarc.gsfc.nasa.gov/W3Browse/fermi/fermigbrst.html.

[b] From M. Ajello et al. (2019).

[c] From A. Y. Lien et al. (2021) in the 15–350 keV range.

[d] From D. Frederiks et al. (2021) in the 20 keV–20 MeV range.

[e] From A. Tsvetkova et al. (2022) in the 20 keV–20 MeV range.

[f] From T. Hussenot-Desenonges et al. (2024) in the 10 keV–1 MeV range.

Table 2
Best-fit Parameters of the Temporal and Spectral Indices from the X-Ray Analysis

GRB Name	X-Ray LC Best-fit Model	$\alpha_{X_1} \pm \delta_{\alpha_{X_1}}$	$\alpha_{X_2} \pm \delta_{\alpha_{X_2}}$	$\alpha_{X_3} \pm \delta_{\alpha_{X_3}}$	$\alpha_{X_4} \pm \delta_{\alpha_{X_4}}$	$\alpha_{X_5} \pm \delta_{\alpha_{X_5}}$	$\beta_{X_1} \pm \delta_{\beta_{X_1}}$	$\beta_{X_2} \pm \delta_{\beta_{X_2}}$	$\beta_{X_3} \pm \delta_{\beta_{X_3}}$	$\beta_{X_4} \pm \delta_{\beta_{X_4}}$	$\beta_{X_5} \pm \delta_{\beta_{X_5}}$
090328A	PL	⋯	⋯	⋯	⋯	1.64 ± 0.07	⋯	⋯	⋯	⋯	0.97 ± 0.24
090510A	BPL	⋯	⋯	⋯	0.63 ± 0.04	2.06 ± 0.08	⋯	⋯	⋯	0.64 ± 0.12	0.86 ± 0.18
090902B	PL	⋯	⋯	⋯	⋯	1.33 ± 0.03	⋯	⋯	⋯	⋯	0.76 ± 0.12
090926A	PL	⋯	⋯	⋯	⋯	1.43 ± 0.03	⋯	⋯	⋯	⋯	1.03 ± 0.12
120711A	PL	⋯	⋯	⋯	⋯	1.60 ± 0.01	⋯	⋯	⋯	⋯	0.82 ± 0.08
130427A	PL+BPL+PL	⋯	2.099 ± 0.002	0.94 ± 0.01	1.45 ± 0.08	1.28 ± 0.01	⋯	0.61 ± 0.02	0.50 ± 0.02	0.85 ± 0.17	0.70 ± 0.04
141028A	PL	⋯	⋯	⋯	⋯	0.92 ± 0.26	⋯	⋯	⋯	⋯	1.00 ± 0.45
160625B	BPL	⋯	⋯	⋯	1.27 ± 0.12	2.13 ± 0.89	⋯	⋯	⋯	0.66 ± 0.52	0.80 ± 0.35
170405A	PL+BPL	⋯	⋯	1.98 ± 0.04	0.95 ± 0.14	1.83 ± 0.17	⋯	⋯	0.62 ± 0.16	0.85 ± 0.09	1.20 ± 0.50
171010A	BPL	⋯	⋯	⋯	1.34 ± 0.04	1.94 ± 0.17	⋯	⋯	⋯	0.93 ± 0.15	0.61 ± 0.29
180720B	PL+BPL+BPL	0.980 ± 0.009	0.53 ± 0.02	1.16 ± 0.09	2.16 ± 2.48	1.51 ± 2.46	0.70 ± 0.02	0.70 ± 0.02	0.76 ± 0.04	⋯	0.74 ± 0.06
210822A	PL+BPL	⋯	⋯	1.03 ± 0.09	1.13 ± 0.04	1.82 ± 0.05	⋯	⋯	0.74 ± 0.02	0.60 ± 0.12	0.78 ± 0.11
220101A	PL+BPL+PL	⋯	0.04 ± 0.07	1.084 ± 0.004	1.18 ± 0.05	1.70 ± 1.50	⋯	-0.07 ± 0.03	0.68 ± 0.19	0.63 ± 0.04	0.86 ± 0.10
230812B	PL	⋯	⋯	⋯	⋯	1.28 ± 0.04	⋯	⋯	⋯	⋯	0.74 ± 0.15

Note. Columns (1) and (2): GRB names and the best-fit model, respectively. Columns (3) and (7): first temporal slope of the PL+BPL+PL fit, α_{X_1}à, and the corresponding spectral parameter, β_{X_1}, respectively. Columns (4) and (8): second temporal slope of the PL+BPL+PL fit, α_{X_2}, and the corresponding spectral parameter, β_{X_2}, respectively. Columns (5) and (9): third temporal slope of the PL+BPL+PL fit, α_{X_3}, and the corresponding spectral parameter, β_{X_3}, respectively. Columns (6) and (10): fourth temporal slope of the PL+BPL+PL fit, α_{X_4}, and the corresponding spectral parameter, β_{X_4}, respectively.

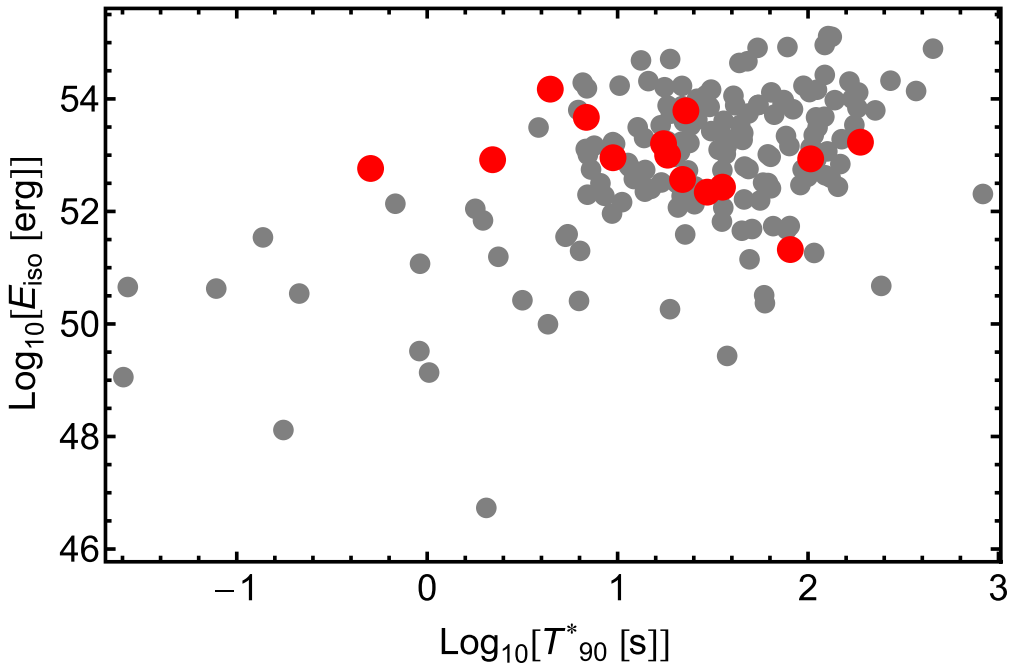

Figure 2. The distribution of $\log(E_{\rm iso})$ vs. $\log(T^*_{90})$ for the bursts in our sample (large red dots), together with all other GRBs with redshifts reported in the Fermi-GBM catalog (gray dots). Quantities marked with "*" refer to rest-frame-calculated values.

3. Methodology

3.1. Data Analysis

We performed fitting of the GRB LCs with the simple PL and the BPL model or combinations thereof. The PL function describing the temporal evolution of the GRB flux is defined as follows:

$$F(t) = F_0\left(\frac{t}{T_0}\right)^{-\alpha}, \tag{1}$$

where F_0 represents the normalization flux, T_0 represents the GRB trigger time, t represents the time of the observation relative to T_0, and α indicates the temporal decay index. The BPL function, on the other hand, is expressed as follows:

$$F(T) = F_b\begin{cases}\left(\frac{t}{T_b}\right)^{-\alpha_1} & t < T_b,\\ \left(\frac{t}{T_b}\right)^{-\alpha_2} & t \geqslant T_b\end{cases} \tag{2}$$

where T_b represents the break time, F_b represents the flux at T_b, and α_1 and α_2 denote the temporal decay indices before and after T_b, respectively. For Fermi-LAT, we used the values for α_γ and β_γ given in M. Ajello et al. (2019), which are based on either a PL model (seven GRBs) or a BPL model (seven GRBs). In the case of X-rays, we employ the `grbLC` package, an automated LC fitting tool (M. G. Dainotti et al. 2024), to determine the best-fit model among the different models (PL, BPL, or their combinations). We performed different fittings and decided which is the best fit based on a comparison among models. This comparison was performed in several steps. First, we found the minimum of the Akaike information criterion (AIC; H. Akaike 1974) among the considered models, denoted by $\rm AIC_{min}$. Then, we computed the $B_{\rm i} = e^{(\rm AIC_{min} - AIC_i)/2}$ for each model, where $B_{\rm i}$ is the Akaike model weight, and $\rm AIC_i$ refers to the AIC of the respective model. Finally, for every model we determined the relative likelihood, denoted as $p_{\rm i} = B_{\rm i} \,/\, \sum_{\rm i} (B_{\rm i})$, where the sum is taken over all models under consideration. The model with $p > 0.95$ is chosen as the best-fit LC model. For GRBs where none of the fitting models achieves a p-value greater than 0.95, we manually select the best-fit model by examining the contour plots. This manual inspection allows us to determine the most suitable model visually. Based on the best-fit model, we extracted the value of $\alpha_{\rm X}$. Subsequently, we obtained the value of the photon index gamma ($\Gamma_{\rm X}$) from the Swift repository by using time-sliced spectra, which correspond to the time range of the several segments of the LC.[11] Finally, we calculated $\beta_{\rm X}$ as $\Gamma_{\rm X} = \beta_{\rm X} - 1$. For the optical data, as they were taken from M. G. Dainotti et al. (2024), the LC data had already been stacked together to allow better coverage of the LCs. To stack the data, we followed several steps, following M. G. Dainotti et al. (2024). First, we flagged the outliers "yes" in the initial magnitude data. We classify outliers into three categories: bad photometry points, where the photometry is deemed unreliable according to their sources (e.g., some GCNs); data points with magnitudes that deviate by at least 5σ from other data points at the same epoch; nonsimultaneous outliers, for which the coincident epoch criterion (as defined in Equation (3) taken from M. G. Dainotti et al. 2024) cannot be applied, and their magnitudes deviate by more than 5σ from the closest data points in time (M. G. Dainotti et al. 2024).

The coincident criterion is defined as follows:

$$\frac{|t_f - t_g|}{t_f} \leqslant 0.025 \longrightarrow t_f \text{ and } t_g \text{ are coincident}, \tag{3}$$

[11] https://www.swift.ac.uk/burst_analyser/

Table 3
Best-fit Models from the X-Ray Analysis

GRB Name	X-Ray LC Best-fit Model	$\log(t_{\rm start})$ (s)	$\log(t_{\rm end})$ (s)	$\log(t_{\rm break_1})$ (s)	$\log(t_{\rm break_2})$ (s)	$\log(t_{\rm break_3})$ (s)	$\log(t_{\rm break_4})$ (s)	$\log(t_{\rm start,EI})$ (s)	$\log(t_{\rm end,EI})$ (s)	$t_{\rm plateau}$ (s)
090328A	PL	4.76	5.90	⋯	⋯	⋯	⋯	4.76	5.90	5.87
090510A	BPL	2.00	4.80	⋯	3.13 ± 0.05	⋯	⋯	2.00	3.13 ± 0.05	3.10
090902B	PL	4.67	6.20	⋯	⋯	⋯	⋯	4.67	6.2	6.19
090926A	PL	4.67	6.29	⋯	⋯	⋯	⋯	4.67	6.29	6.28
120711A	PL	3.89	5.39	⋯	⋯	⋯	⋯	3.9	5.39	5.38
130427A	PL+BPL+PL	2.20	7.19	2.782 ± 0.006	3.77 ± 0.18	4.90 ± 0.40	⋯	2.782 ± 0.06	3.77 ± 0.18	3.72
141028A	PL	4.50	5.08	⋯	⋯	⋯	⋯	4.50	5.08	4.95
160625B	BPL	3.99	6.59	⋯	6.26 ± 1.14	⋯	⋯	3.99	6.26 ± 1.14	6.26
170405A	PL+BPL	2.30	5.04	2.84 ± 0.04	3.76 ± 0.19	⋯	⋯	2.84	3.76 ± 0.19	3.70
171010A	BPL	4.39	6.21	⋯	5.54 ± 0.14	⋯	⋯	4.39	5.54 ± 0.14	5.51
180720B	PL+BPL+BPL	2.30	6.46	3.020 ± 0.009	3.32 ± 0.11	4.71 ± 0.94	4.72 ± 0.94	3.020 ± 0.009	3.32 ± 0.11	3.02
210822A	PL+BPL	1.80	5.70	2.75 ± 0.38	4.06 ± 0.07	⋯	⋯	2.75 ± 0.38	4.06 ± 0.07	4.04
220101A	PL+BPL+PL	1.87	6.04	2.141 ± 0.009	3.59 ± 0.28	4.89 ± 0.04	⋯	3.59 ± 0.28	4.89 ± 0.04	4.87
230812B	PL	4.39	6.19	⋯	⋯	⋯	⋯	4.39	6.19	6.18

Note. Columns (1) and (2): GRB names and the best-fit model, respectively. Columns (3) and (4): start and end times of the LC, respectively. Column (5): time at the end of the PL and the start of the BPL for the case of PL+BPL, PL+BPL+PL, and PL+BPL+BPL. Column (6): break time between the two segments of the BPL in the case of BPL, PL+BPL, PL+BPL+PL, and PL+BPL+BPL. Column (7): time at the end of the BPL and the start of the PL and BPL in the case of PL+BPLP+PL and PL+BPL+BPL. Column (8): break time between the two segments of the second BPL in the case of PL+BPL+BPL. Columns (9) and (10): start and end times of the energy injection, respectively. Column (11): duration of the plateau.

where t_f and t_g represent the midpoints of the observations in the given filter band, denoted with f, and g denotes a generic band from which we start the calculation, respectively, measured in seconds after the satellite trigger. In our case, we are rescaling in the R band. Second, we remove these outliers' data points. Third, we convert the magnitudes into the AB system. Fourth, we correct for the Galactic extinction. Fifth, we apply a k-correction. And sixth, we undertake the color evolution analysis (M. G. Dainotti et al. 2024).

Here, we define color evolution as the changes in color over time. More specifically, the color is the difference in magnitude between two bands, one of which serves as a reference at a specific time. To investigate whether a GRB displays color evolution, we first compute the rescaling factors using Equation (4), taken from M. G. Dainotti et al. (2024):

$$rf_{mn,f} = a * \log_{10}(t_f) + b, \tag{4}$$

where f denotes the f band, mn represents the most numerous filter, a is the slope, and b is the normalization. This equation is computed for each data point, allowing us to analyze the behavior across different filters. The rescaling factor is fitted with slope $a = 0$ and normalization b. We then calculate the probability P that the fitting is drawn by chance, the reduced χ^2, and the Bayesian information criterion value. If $P \geqslant 0.05$, we categorize the GRB as exhibiting no color evolution. Conversely, if $P < 0.05$, the GRB is considered to exhibit color evolution. We then stacked the LCs in different bands only when no color evolution was detected among the bands; we removed those filters that exhibit color evolution. Finally, we converted the magnitudes into flux for proceeding with the LC fitting to obtain the $\alpha_{\rm opt}$ parameter. We followed the same approach for fitting the optical LCs as used for the X-ray LC fitting. The $\beta_{\rm opt}$ values were obtained from M. G. Dainotti et al. (2024). Tables 1, 2, and 4 display the GRB sample used in this study and their best-fit models for the gamma-ray, X-ray, and optical LCs, respectively. The tables also present each wavelength's corresponding α and β values. In Tables 1 and 4, we also provide the start and end times of the LC and the break times for gamma-ray and optical LCs, respectively. Table 1 also details the energy injection time and the duration of the plateau for gamma-ray LCs. Table 3 details the start and end times of the X-ray LCs along with the break time, the energy injection time, and the duration of the plateau. Table 5 presents the energy injection time and the duration of the plateau for optical LCs.

3.2. Derivation of the Bulk Lorentz Factor

We here derive the equation for the bulk Lorentz factor in a stratified density profile ($=A_k \times r^{-k}$) for $0 \leqslant k < 3$.

During the deceleration phase, the bulk Lorentz factor of the relativistic outflow becomes $E_k = \frac{4\pi}{3} m_p c^2 n(r) r^3 \Gamma^2$ (Blandford–McKee solution; R. D. Blandford & C. F. McKee 1976), with the radial distance given by

$$r \simeq \frac{2c}{1+z}\Gamma^2 t. \tag{5}$$

This equation considers the approximation of the volume of the expanding plasma with a sphere shape. We then substitute $n(r)$ and r in the Blanford–Mckee solution, and obtain

$$E_k = \frac{4\pi}{3}(2c)^{3-k} m_p c^2 (1+z)^{3-k} A_k \Gamma^{8-2k} t^{3-k} 4. \tag{6}$$

Table 4
Best-fit Parameters of the Optical Temporal and Spectral Analysis

GRB Name	Optical LC Best-fit Model	$\alpha_{\mathrm{opt}_1} \pm \delta_{\alpha_{opt1}}$	$\alpha_{\mathrm{opt}_2} \pm \delta_{\alpha_{\mathrm{opt}2}}$	$\alpha_{\mathrm{opt}_3} \pm \delta_{\alpha_{opt3}}$	$\beta_{\mathrm{opt}} \pm \delta_{\beta_{\mathrm{opt}}}$	β_{opt} Source	$\log(t_{\mathrm{start}})$ (s)	$\log(t_{\mathrm{end}})$ (s)	$\log(t_{\mathrm{break_1}})$ (s)	$\log(t_{\mathrm{break_2}})$ (s)
090328A	PL	⋯	⋯	0.95 ± 0.09	1.19 ± 0.21	L. Li et al. (2012)	4.76	6.03	⋯	⋯
090510A	BPL	⋯	6.96 ± 1.56	2.57 ± 0.69	0.85 ± 0.05	L. Li et al. (2018a)	4.35	4.55	⋯	4.38 ± 0.04
090902B	BPL	⋯	2.16 ± 1.64	0.77 ± 0.07	0.68 ± 0.11	L. Li et al. (2012)	3.72	6.01	⋯	4.41 ± 0.30
090926A	BPL	⋯	0.003 ± 0.213	1.34 ± 0.16	0.72 ± 0.17	L. Li et al. (2012)	4.84	5.98	⋯	4.96 ± 0.09
120711A	PL+BPL	1.75 ± 0.02	0.37 ± 0.04	1.48 ± 0.08	0.53 ± 0.02	L. Li et al. (2018a)	2.11	5.57	3.19 ± 0.04	4.78 ± 0.05
130427A	PL+BPL	1.19 ± 0.04	1.000 ± 0.002	0.33 ± 0.04	0.92 ± 0.10	L. Li et al. (2018a)	2.64	8.0	3.07 ± 0.04	6.00 ± 0.02
141028A	PL	⋯	⋯	1.01 ± 0.08	1.29 ± 0.07	J. M. Burgess et al. (2016)	4.57	5.18	⋯	⋯
160625B	BPL	⋯	0.949 ± 0.007	1.54 ± 0.06	0.68 ± 0.07	T. Kangas et al. (2020)	4.51	6.67	⋯	6.13 ± 0.033
170405A	PL	⋯	⋯	1.38 ± 0.12	0.80 ± 0.09	M. G. Dainotti et al. (2022c)	2.31	3.77	⋯	⋯
171010A	BPL	⋯	6.68 ± 0.28	0.10 ± 0.01	1.33 ± 0.19	A. Melandri et al. (2019)	5.11	7.01	⋯	5.56 ± 0.05
180720B	PL	⋯	⋯	0.87 ± 0.04	0.80 ± 0.04	N. Fraija et al. (2019)	4.01	4.60	⋯	⋯
210822A	PL	⋯	⋯	1.34 ± 0.02	0.77 ± 0.03	C. Angulo-Valdez et al. (2024)	2.25	2.97	⋯	⋯
220101A	BPL	⋯	2.39 ± 0.18	0.47 ± 0.14	0.70 ± 0.05	Z.-P. Jin et al. (2023)	2.2	4.8	⋯	3.28 ± 0.12
230812B	PL+BPL	1.44 ± 0.02	0.016 ± 0.011	3.45 ± 0.52	0.74 ± 0.02	G. P. Srinivasaragavan et al. (2024)	4.48	6.52	5.46 ± 0.01	6.29 ± 0.01

Note. Columns (1) and (2): GRB names and the best-fit model, respectively. Columns (3), (4), and (5): the first temporal slope of the PL+BPL fit (α_{opt_1}), the second temporal slope of the PL+BPL fit (α_{opt_2}), and the third temporal slope of the PL+BPL fit (α_{opt_3}) , respectively. Column (6): spectral parameter, β_{opt}, which is considered to be the same for all segments of the LCs. Column (7): references from where the β_{opt} has been extracted. Columns (8) and (9): start and end times of the LC, respectively. Column (10): time at the end of the PL and the start of the BPL in the case of PL+BPL ($\log t_{\mathrm{break_1}}$) and its uncertainty. Column (11): break time between the two segments of the BPL in the case of both BPL and PL+BPL $\log t_{\mathrm{break_2}}$ and its uncertainty.

Table 5
Best-fit Models from the Optical Analysis

GRB Name	z	Source	Optical LC	$\log(t_{\rm start,EI})$ (s)	$\log(t_{\rm end,EI})$ (s)	$\log(t_{\rm plateau})$ (s)
090328A	0.736	JG[a]	PL	4.76	6.03	6.00
090510A	0.903	Very Large Telescope (VLT) emission[b]	BPL	4.38 ± 0.04	4.55	4.06
090902B	1.822	JG[a]	BPL	4.42 ± 0.30	6.01	6.00
090926A	2.106	JG[a]	BPL	4.96 ± 0.09	5.98	5.94
120711A	1.405	JG[a]	PL+BPL	3.19 ± 0.035	4.78 ± 0.05	4.77
130427A	0.339	Gemini North absorption[b]	PL+BPL	3.07 ± 0.04	6.00 ± 0.02	6.00
141028A	2.330	JG[a]	PL	…	…	…
160625B	1.406	JG[a]	BPL	4.51	6.13 ± 0.03	6.12
170405A	3.510	GTC absorption[b]	PL	2.31	3.77	3.75
171010A	0.329	JG[a]	BPL	…	…	…
180720B	0.654	VLT absorption[b]	PL	…	…	…
210822A	1.736	NOT absorption[b]	PL	…	…	…
220101A	4.618	NOT absorption[b]	BPL	3.28 ± 0.12	4.08	4.01
230812B	0.360	JG[a]	PL+BPL	5.46 ± 0.01	6.29 ± 0.01	6.22

Notes. Columns (1), (2), (3), and (4): GRB name, redshift, source for the redshift, and best-fit model, respectively. Columns (5) and (6): energy injection start and end times, respectively. Column (7): duration of the plateau in log scale.
[a] From https://www.mpe.mpg.de/jcg/grbgen.html.
[b] From https://swift.gsfc.nasa.gov/archive/grb_table/.

Now, we solve for Γ:

$$\Gamma = \left(\frac{3}{4\pi m_p c^2 (2c)^{3-k}}\right)^{\frac{1}{2(4-k)}} (1+z)^{\frac{3-k}{2(4-k)}} A_k^{-\frac{1}{2(4-k)}} E_k^{\frac{1}{2(4-k)}} t^{-\frac{(3-k)}{2(4-k)}}. \quad (7)$$

From this equation, we can compute the bulk Lorentz factor by considering the time we are in the emission and then substitute this value in Equation (5).

3.3. Testing the Closure Relations

We followed a similar approach to M. Dainotti et al. (2023) for comprehensively examining CRs between α and β. These CRs are associated with different astrophysical environments, including the density profile of the surrounding medium, the p index, and the electron cooling regime. Furthermore, we examined three sets of CRs: one with energy injection, one with no energy injection, and the other for the jet break. We have also taken into account different density profiles encompassing a constant-density ISM characterized by $n \propto r^0$, a stellar wind medium, $n \propto r^{-2}$, and a stratified density profile, $n \propto r^{-k}$, with k values of 1, 1.5, and 2.5.

Prior studies conducted by P. Kumar & T. Piran (2000), P. A. Crowther (2007), F. De Colle et al. (2012a, 2012b), K. Hotokezaka et al. (2013), S.-X. Yi et al. (2013, 2020), and M. Dainotti et al. (2023) have thoroughly discussed the presence of a stratified medium. In this study, we tested $k = 0$, 1, 1.5, 2, and 2.5 for both the energy-injection and no-energy-injection scenarios considering three regimes: slow-cooling (SC; $\nu_m < \nu < \nu_c$), fast-cooling (FC; $\nu_c < \nu < \nu_m$), and slow/fast-cooling (SC/FC; $\nu > \max\{\nu_c, \nu_m\}$). We adopted the set of CRs for the no-energy-injection scenario for $k = 0$ and 2 from G. P. Srinivasaragavan et al. (2020), whereas the set of CRs that account for energy injection was adopted from J. L. Racusin et al. (2009) and H. Gao et al. (2013). The CRs were taken from M. Dainotti et al. (2023) for other density profiles. In our analysis, we analyze two sets of electron spectral distribution (p) values for CRs without energy injection: one for $1 < p < 2$, and the other for $p > 2$. However, for CRs with energy injection, we exclusively focus on the p value where $p > 2$, following J. L. Racusin et al. (2009). For GRBs detected by Fermi-LAT, we use α_{γ_2} when a GRB is fitted with a PL, regardless of whether it is in the context of the energy-injection or no-energy-injection scenarios. However, in the case when a GRB is fitted with a BPL, we employ α_{γ_2} when we examine the scenario without energy injection and α_{γ_1} when energy injection is taken into account. The latter scenario indeed happens earlier in time in the segments of the LC. For the X-ray analysis, we utilize different $\alpha_{\rm X}$, depending on the specific GRB and the scenario of energy injection. For GRBs fitted with a PL, we employ $\alpha_{\rm X_5}$ in both scenarios, with and without energy injection. However, for GRBs 090510A and 170405A, we use $\alpha_{\rm X_5}$ when there is no energy injection, and $\alpha_{\rm X_4}$ when energy injection is considered. In the cases of GRBs 130427A and 220101A, $\alpha_{\rm X_4}$ is used for scenarios without energy injection, while $\alpha_{\rm X_3}$ and $\alpha_{\rm X_2}$ are applied when energy injection is considered, respectively. For GRB 180720B, $\alpha_{\rm X_3}$ and $\alpha_{\rm X_2}$ are used for the no-energy-injection and energy-injection cases, respectively. For GRB 210822A, $\alpha_{\rm X_5}$ is used for the no-energy-injection scenario, as it does not exhibit energy injection in its LC. Similarly, GRBs 160625B and 171010A show no signs of energy injection; hence, $\alpha_{\rm X_4}$ is used for their analysis in the absence of energy injection. For the optical analysis, we also employ different $\alpha_{\rm opt}$, depending on the specific GRB and the scenario of energy injection. In cases where the GRB is fitted with a PL, $\alpha_{\rm opt_3}$ is applied consistently across both scenarios, whether energy injection is present or not. However, for GRBs 090510A, 090902B, 130427A, 160625B, 171010A, and 220101A, $\alpha_{\rm opt_2}$ is used exclusively under the no-energy-injection scenario, as these GRBs do not show evidence of energy injection in their LCs. For GRBs 090926A, 120711A, and 230812B, $\alpha_{\rm opt_3}$ is used when there is no energy injection, whereas $\alpha_{\rm opt_2}$ is utilized when a scenario with energy injection is taken into account. We show the GRB LCs of our sample in all wavelengths in

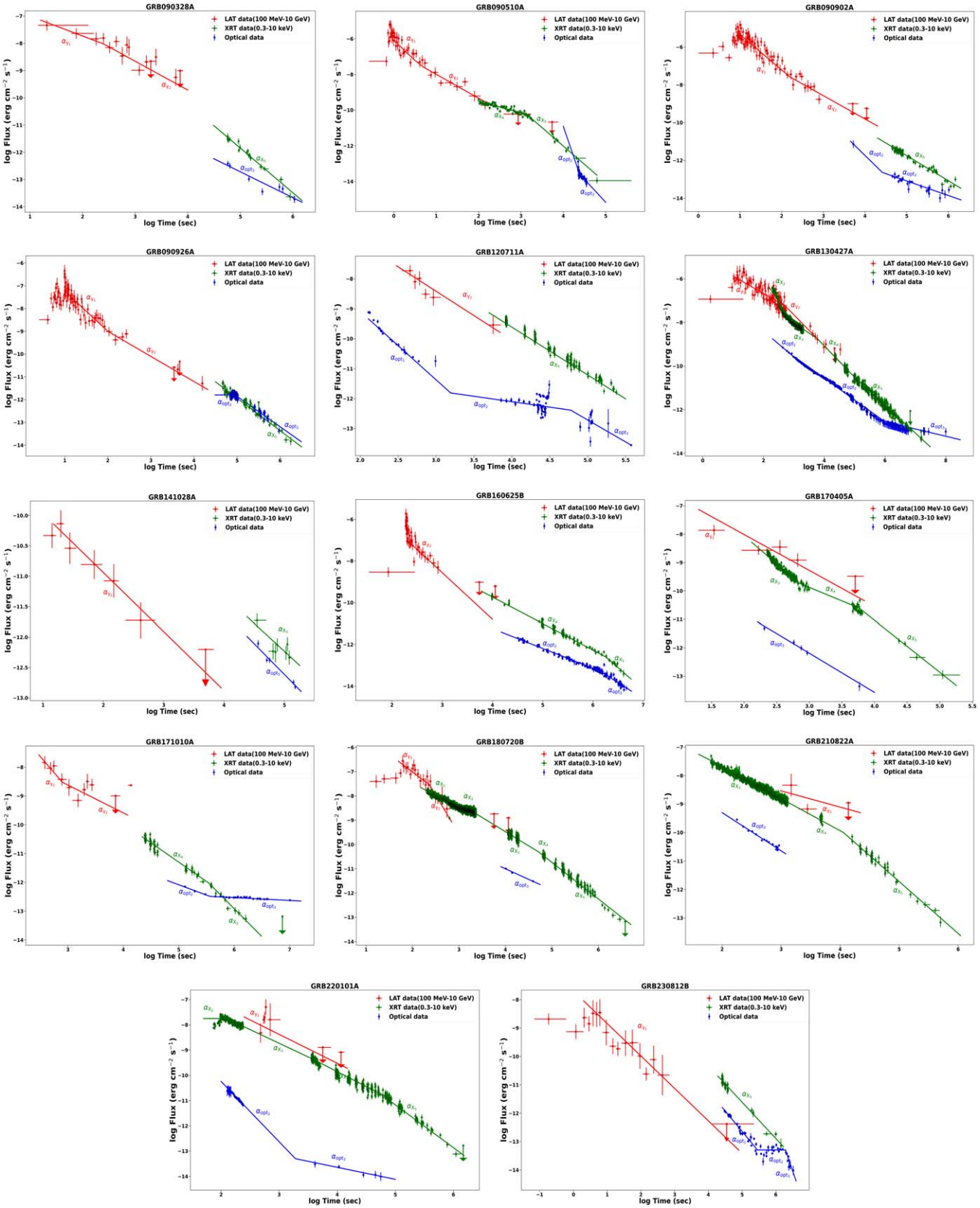

Figure 3. Comprehensive LCs of 14 GRBs from our sample spanning across gamma-ray, X-ray, and optical wavelengths merged into a single plot. The corresponding fitting slopes (α) with respect to each wavelength are also indicated in the plot.

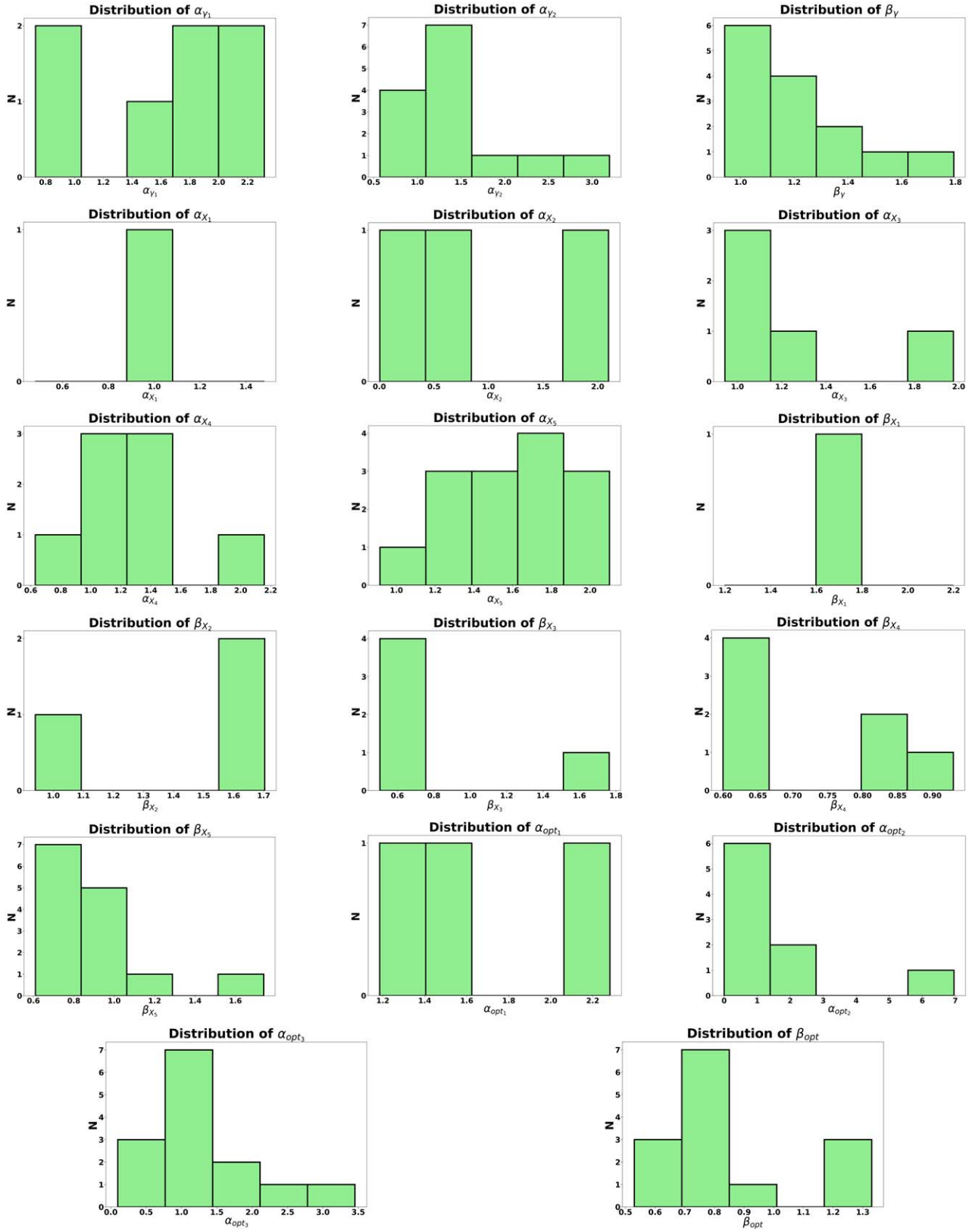

Figure 4. Distribution of α and β parameters across gamma rays, X-rays, and the optical band for the 14 GRBs used in this study.

Figure 3, where the X-ray LCs of GRBs 090510A, 090926A, 141028A, 170405A, and 230812B are rescaled for visualization purposes to their respective gamma-ray LCs; others remain unrescaled. In Figure 4, we show the distributions of the α_{γ_1}, α_{γ_2}, β_γ, α_{X_1}, α_{X_2}, α_{X_3}, α_{X_4}, α_{X_5}, β_{X_1}, β_{X_2}, β_{X_3}, β_{X_4}, β_{X_5}, α_{opt_1}, α_{opt_2}, α_{opt_3}, and β_{opt} parameters in our sample.

In our analysis of CRs, we also consider the jet-break scenario, using jet-break equations derived from N. Fraija et al. (2022b),

which are quoted in Equation (8):

$$F_\nu \propto \begin{cases} t^{-1}\nu^{-\frac{1}{2}}, & \nu_c < \nu < \nu_m \\ t^{-p}\nu^{-\frac{(p-1)}{2}}, & \nu_m < \nu < \nu_c \\ t^{-p}\nu^{-\frac{p}{2}}, & \max\{\nu_m, \nu_c\} < \nu \end{cases} . \quad (8)$$

It is important to highlight that these jet-break equations are independent of k. Although not all GRBs exhibit a jet break in their LCs, for those that do we apply the specific α parameters to account for the jet break in our CRs. Regarding X-rays, GRBs 130427A, 160625B, 171010A, 180720B, and 220101A show evidence of a jet break whose slope index is α_{X_5}. Similarly, in the optical band, GRBs 090510A, 090902B, 130427A, 160625B, 171010A, and 220101A exhibit a jet break whose slope index is α_{opt_3}.

4. Results

Here, we present the results of the CRs for each wavelength in separate subsections. Figures 5–10 display the sample of 14 GRBs represented in green. GRBs that satisfy the CRs within errors are depicted in purple. We note that since the uncertainties are correlated, these must be represented with ellipses instead of a rectangular shape. The fulfillment (or not) of the CRs is computed mathematically between the regions of the ellipses and the lines representing the CRs. For better visualization, the points showing the CRs are large. The N symbol in the picture shows the number of GRBs fulfilling that particular CR for each subpanel. For the X-ray and optical, we display consistently in Figures 6–9 the SC regime (first column), FC regime (second column), and SC/FC regime (third column) for the following density media: $k = 0$ (first row), $k = 1$ (second row), $k = 1.5$ (third row), $k = 2$ (fourth row), and $k = 2.5$ (fifth row). For the gamma ray, we exclusively show the SC/FC ($\nu > \max\{\nu_c, \nu_m\}$) regime for all k values (0, 1, 1.5, 2, and 2.5), depicted in Figure 5. In Figure 10, we show the jet-break CRs for X-ray and optical with density medium in the SC regime (first column), FC regime (second column), and SC/FC regime (third column). The CRs are graphically represented in all wavelengths as lines or points depending on the values of α and β. When $p > 2$, CRs are denoted by red lines or points for both with or without energy injection cases. For CRs without energy injection where $1 < p < 2$, they are represented by a blue line or point. CRs with a jet break where $1 < p < 2$ are represented by a red line or point.

4.1. Gamma-Ray Closure Relations

We summarize the CR results for gamma rays in Table 6. We here decide to discuss and present only the SC/FC ($\nu > \max\{\nu_c, \nu_m\}$) regime since the other scenarios carry little information and are less likely to happen in high-energy gamma rays. Under the no-energy-injection scenario, in the SC/FC ($\nu > \max\{\nu_c, \nu_m\}$) regime, three GRBs (21.4%) satisfy the CRs for all values of k. This means that there is a degeneracy among the several possible media. The GRBs are 090926A, 171010A, and 230812B. However, in this scenario only the case of GRB 220101A (7.14%) satisfies the CRs in the energy injection for all the k values.

4.2. X-Ray Closure Relations

In the case of X-rays, Table 7 summarizes the CR results. In the no-energy-injection scenario, the most preferred regime is the SC regime, where nine GRBs (64.3%) in $k = 0$ satisfy the CRs, followed by $k = 1$ and 1.5 with eight GRBs (57.1%), five GRBs (35.7%) for $k = 2$, and one GRB (7.14%) for $k = 2.5$. In this case, the ISM is the most preferred environment.

The second most preferred regime is the SC/FC ($\nu > \max\{\nu_c, \nu_m\}$) regime, where three GRBs (21.4%) satisfy the CRs for all values of k. The least preferred regime is the FC regime ($\nu_c < \nu < \nu_m$) for all k values, with none (0%) of the GRBs satisfying the CRs. Similarly, in the energy-injection scenario, the SC regime is favored the most, with a stratified medium of $k = 2.5$ and a wind medium of $k = 2$ with three GRBs (21.4%) satisfying the CRs, and only one GRB (7.14%) fulfilling the CR for $k = 1.5$. In this case, the most preferred environment is the stratified medium with $k = 2.5$ along with the wind medium. The least preferred regimes are the FC and SC/FC regimes, where no (0%) GRB satisfies the CRs for all values of k.

In the jet-break scenario, the preferred regime is the SC/FC, with two GRBs (14.3%) conforming to the CRs. In this case, both the SC and FC regimes are the least favored regimes, with no (0%) GRBs fulfilling the CRs.

4.3. Optical Closure Relations

For optical wavelengths, Table 8 summarizes the CR results. In the no-energy-injection scenario, the most preferred regime is the SC/FC regime ($\nu > \max\{\nu_c, \nu_m\}$), with three GRBs (21.4%) satisfying the CRs for the $k = 2.5$, followed by the constant medium $k = 0$ and $k = 1$, 1.5, and 2, with only two GRBs (14.3%). In this case, the most preferred environment is the stratified medium with $k = 2.5$. The least preferred regimes are the SC and FC regimes for all k values, with none (0%) of the GRBs satisfying the CRs. However, in the scenario with energy injection, we observe that the most preferred is the SC regime for $k = 1$, 2, and 2.5, with only one GRB (7.14%) satisfying the CRs. For the same regime with $k = 0$, none (0%) of the GRBs conforms to the CRs. The least preferred are the FC and SC/FC regimes, where none (0%) of the GRBs satisfy the CRs for all values of k. Also, in this case, the most preferred environment is the stratified medium with $k = 1$ and 1.5, along with the wind medium. In the jet-break scenario, no (0%) GRBs fulfill the CRs for any regime.

5. Discussion

In Table 9, we present a detailed comparative analysis of each GRB for both of the no-energy-injection (top panel) and energy-injection scenarios (bottom panel), respectively. The individualized comparative analysis provides insights into the energy mechanism and the ambient environment for each GRB across these wavelengths. The table is comprehensive, and thus we omit to discuss the singular cases, but we instead provide pie charts (Figure 12) for the analysis in relation to the density environments.

5.1. The No-energy-injection and Energy-injection Scenarios

To simplify the visualization of the energy-injection and no-energy-injection cases, we show a Venn diagram (see Figure 11) illustrating which GRBs undergo degeneracies. In

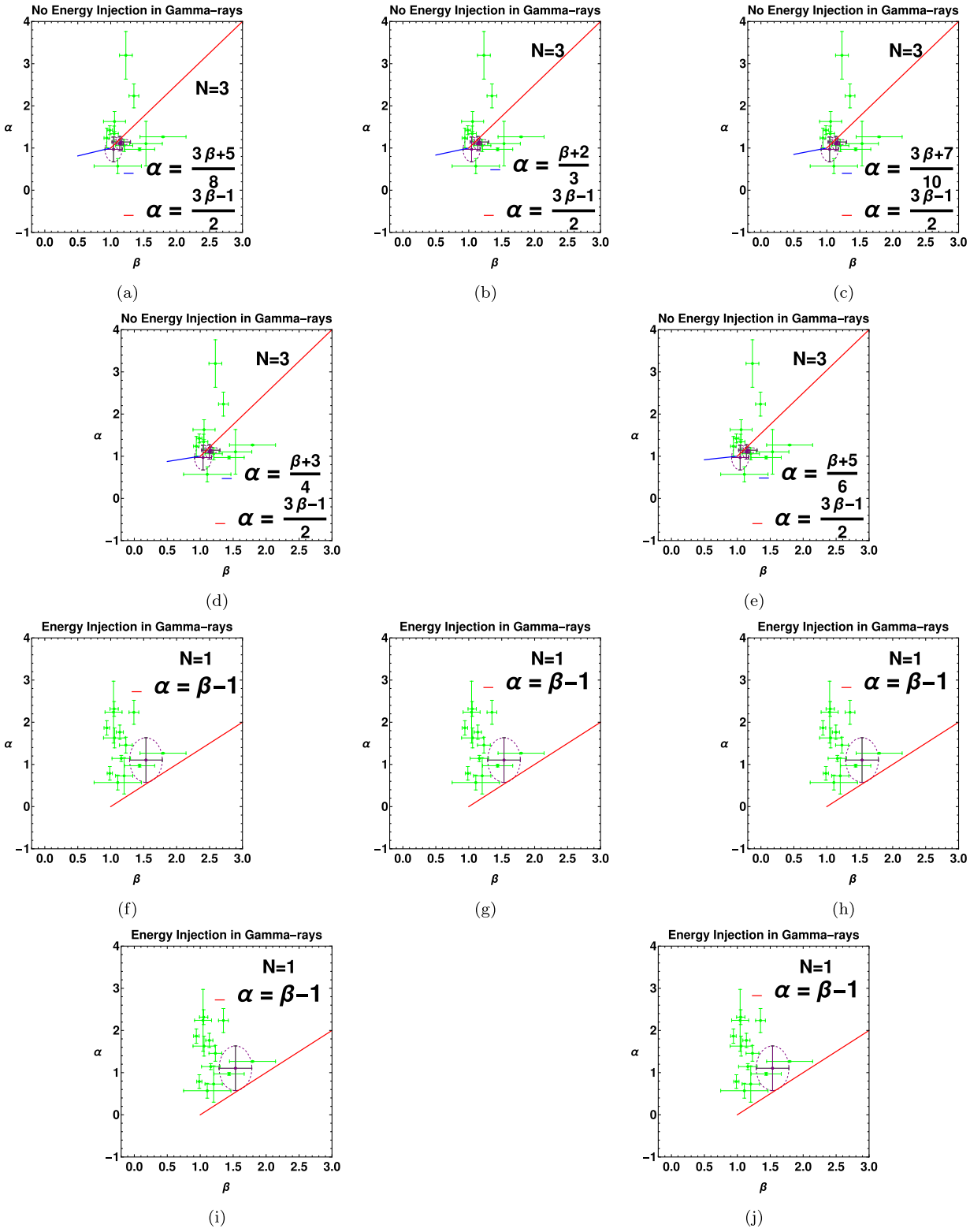

Figure 5. CRs corresponding to the synchrotron FS model for the SC/FC regime for gamma rays. Top two panels: no energy injection ($q = 1$) for $k = 0$–2.5 (from (a) to (e), respectively). Bottom two panels: energy injection ($q = 0$) for $k = 0$–2.5 (from (f) to (j), respectively). GRBs that satisfy the relations for gamma-ray parameters (α_γ and β_γ) are shown in purple; others are shown in green.

the absence of energy injection (see the top panel of Table 9), some GRBs exhibit a preference for a specific value, while some show a preference for more than one value, and some of them have no values for the energy-injection scenario.

Differently from the no-energy-injection scenario, in which all GRBs satisfy at least one CR in at least one energy band, for the case of energy injection there are GRBs for which no CR is fulfilled in any of the bands. These are GRBs 120711A,

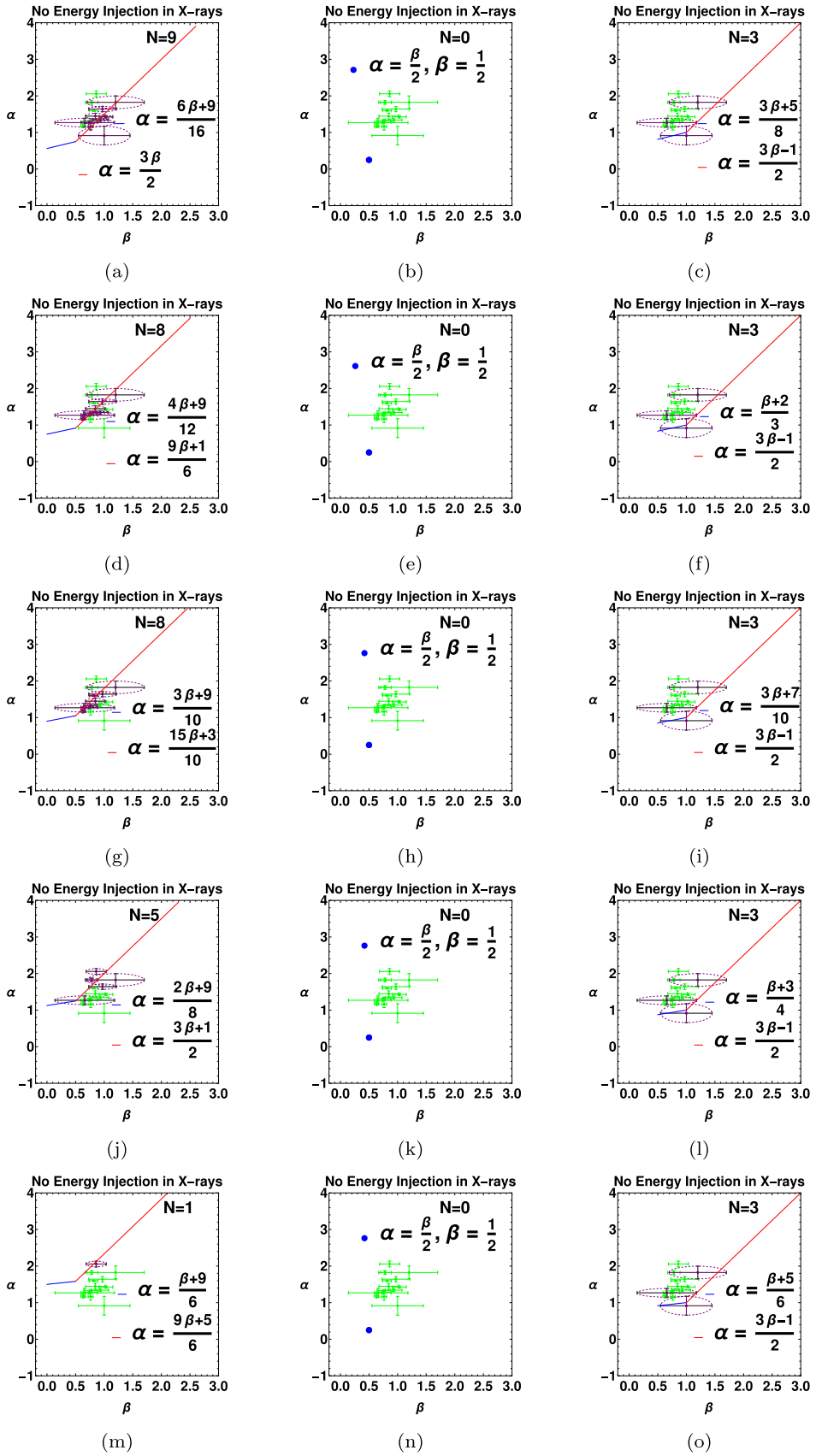

Figure 6. CRs in X-rays corresponding to the synchrotron FS model for $k = 0$–2.5 (from top to bottom) with no energy injection ($q = 1$). Columns denote the SC, FC, and SC/FC regimes, from left to right. GRBs that satisfy the relations for X-ray parameters (α_X and β_X) are shown in purple; others are shown in green.

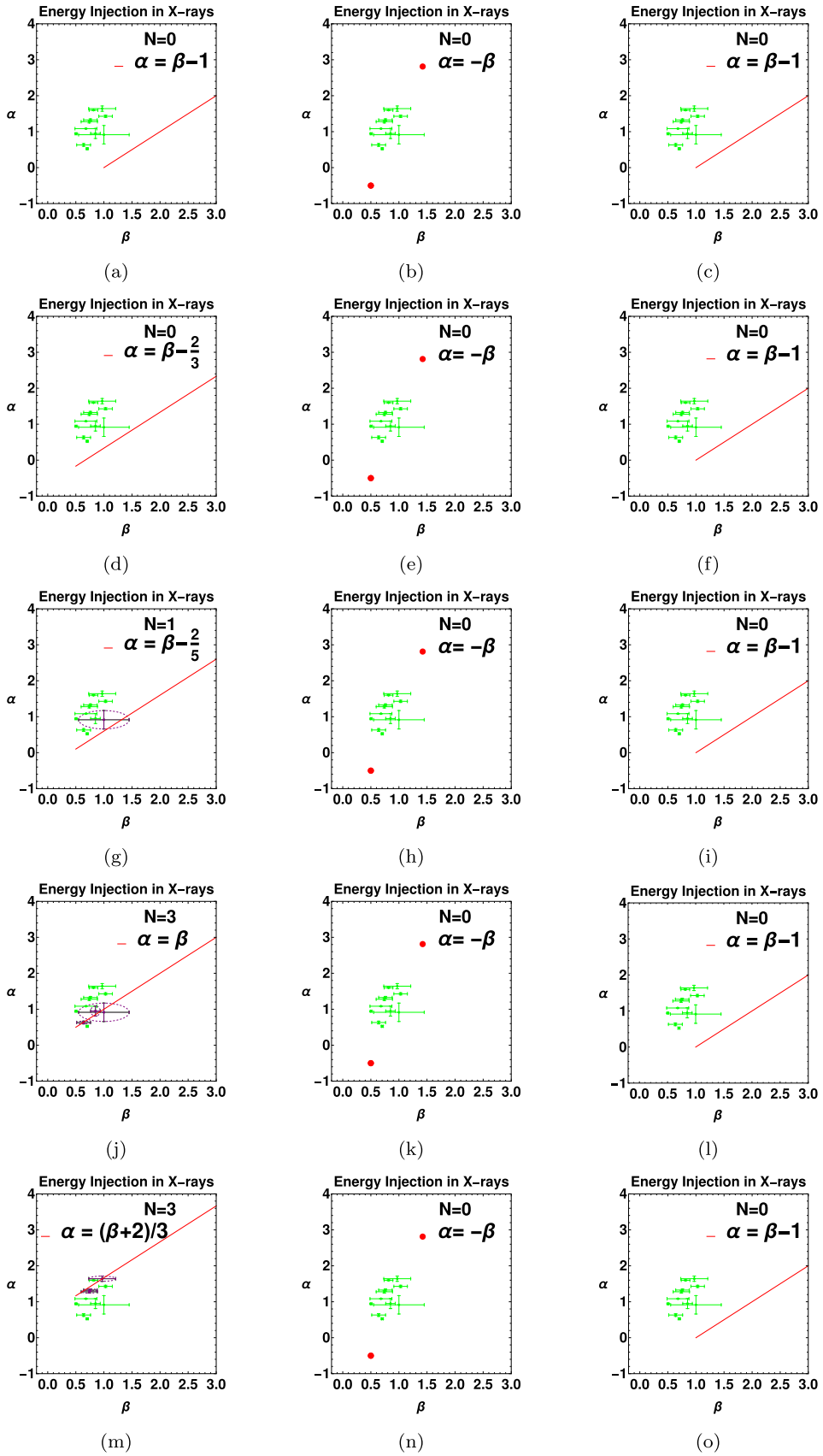

Figure 7. CRs in X-rays corresponding to the synchrotron FS model for $k = 0$–2.5 (from top to bottom) with energy injection ($q = 0$), and $q = 0$ denoting instantaneous energy injection. Columns denote the SC, FC, and SC/FC regimes, from left to right. GRBs that satisfy the relations for X-ray parameters (α_X and β_X) are shown in purple; others are shown in green.

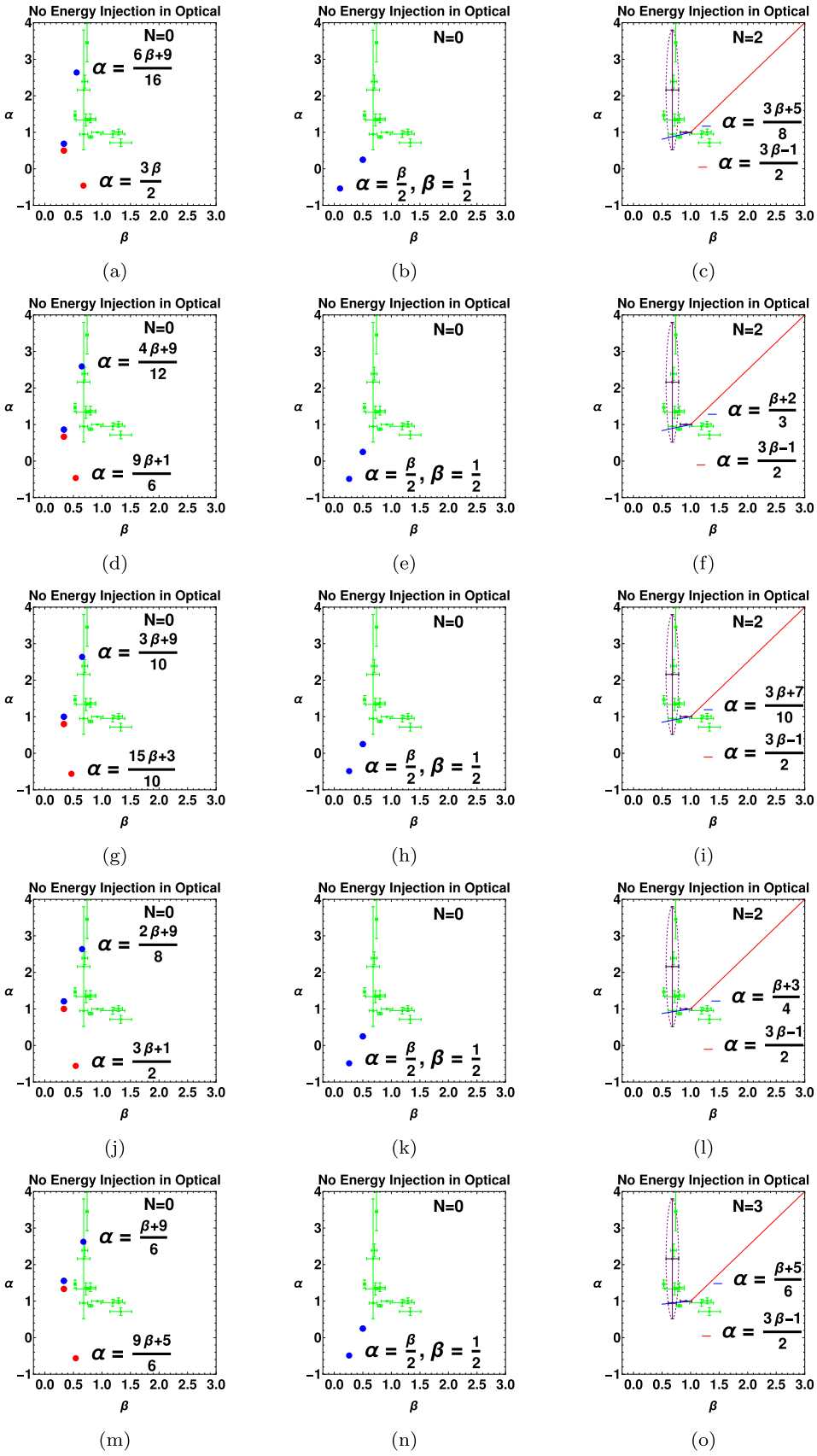

Figure 8. CRs in optical corresponding to the synchrotron FS model for $k = 0$–2.5 (from top to bottom) with no energy injection ($q = 1$). Columns denote the SC, FC, and SC/FC regimes, from left to right. GRBs that satisfy the relations for optical parameters ($\alpha_{\rm opt}$ and $\beta_{\rm opt}$) are shown in purple; others are shown in green.

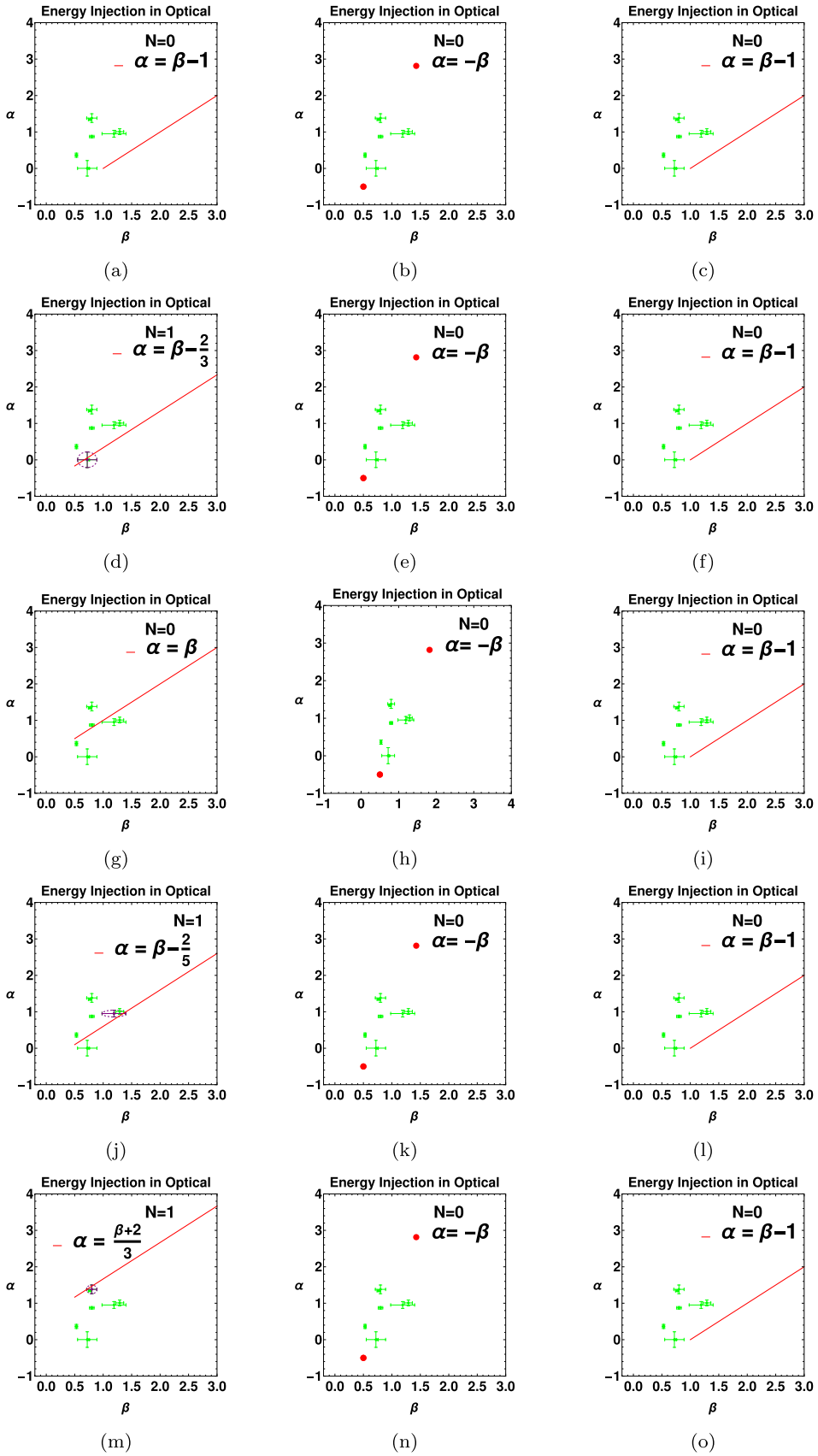

Figure 9. CRs in optical corresponding to the synchrotron FS model for $k = 0$–2.5 (from top to bottom) with energy injection ($q = 0$), and $q = 0$ denoting instantaneous energy injection. Columns denote the SC, FC, and SC/FC regimes, from left to right. GRBs that satisfy the relations for optical parameters ($\alpha_{\rm opt}$ and $\beta_{\rm opt}$) are shown in purple; others are shown in green.

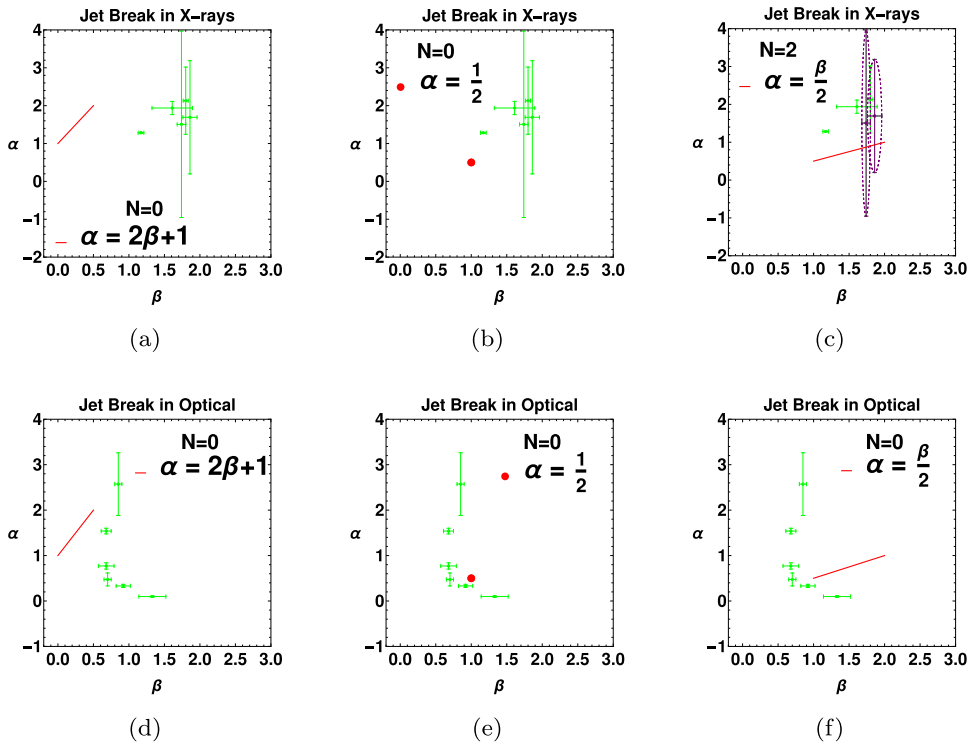

Figure 10. CRs corresponding to the synchrotron FS model with jet break for X-rays (top row) and optical (bottom row). Columns denote the SC, FC, and SC/FC regimes, from left to right. GRBs that satisfy the relations for X-ray parameters (α_X and β_X) and optical parameters (α_{opt} and β_{opt}) are shown in purple; others are shown in green.

130427A, 160625B, 171010A, 180720B, and 210822A. On average, it is evident that CRs without energy injection are preferred over CRs with energy injection.

We have also considered the jet-break scenario, and we notice that the only band in which the CRs are satisfied is in the X-ray, with two cases only for the SC/FC regime.

When considering different cases, our analysis reveals a predominant preference with regard to all wavelengths for the SC/FC ($\nu > \max\{\nu_c, \nu_m\}$) regime in the no-energy-injection scenario, with a total of 36 cases; the second most preferred regime, with 31 cases, is the SC ($\nu_m < \nu < \nu_c$) regime. In the energy-injection scenario, the SC ($\nu_m < \nu < \nu_c$) regime is most preferred, with 10 cases total. In the energy-injection scenario, out of 10 cases, only one is driven by a constant-density medium. In the no-energy-injection scenario, eight out of 36 fulfill the CRs with a constant-density medium. For the optical data only, in the no-energy-injection scenario, 11 cases are fulfilled for the SC/FC regime, with a preference of $k = 2.5$; in the energy-injection scenario, the preferred scenario is the one with a stratified medium for $k = 1$ and 2.5, and it also equivalently prefers a wind medium. In the analysis of optical data, an identical outcome for the $k = 2$ and ISM was found in the investigation conducted by M. G. Dainotti et al. (2022a).

5.2. Discussion Regarding the Environment

One necessary takeaway from this study is that we could pinpoint a definite environment for some GRBs. Two pie charts in Figure 12 show the GRB names along with their corresponding k values, color-coded for both the no-energy-injection (upper panel) and energy-injection (lower panel) scenarios. In the no-energy-injection regime, GRB 120711A has $k = 1.5$, GRB 180720B has $k = 0$, and GRB 210822A has $k = 2$, while other cases are degenerate in the density profile. However, if we explore the energy-injection scenario, the following GRBs have a definite medium: GRB 090510A has $k = 2$ (but also 2.5 in the no-energy-injection scenario), GRB 090902B has $k = 2.5$, GRB 090926A has $k = 1$, and GRB 230812B has $k = 2$. The result for GRB 090510A agrees with A. Panaitescu (2011), who modeled the multiwavelength observations with a stratified medium. We here stress that we have provided in Equation (7) the relation between the Lorentz Γ factor and the kinetic energy, the density profile, and redshift. Thus, one can infer the radii at which the model is a valid approximation. For example, if we consider GRB 130427's time of the last break $t_{break_3} = 80,909$ s and a Lorentz factor of 455, as stated in M. Ackerman et al. (2013), we will obtain a radius of 7.36×10^{20} cm. This would be the radius at which there will be a transition toward the interstellar environment about this GRB, and the radius from the progenitor will be marked as the model of the stratified medium that can still be applicable. This is roughly the order of magnitude for the radii of the other GRBs.

5.3. Comparison with Other Studies

The fact that the no-energy-injection scenario is favored is an exciting conclusion drawn from our study, since many works have invoked the energy-injection scenario to interpret the plateau phase observed in GRB afterglows, especially for Swift-XRT LCs, but also for the high-energy component observed in Fermi-LAT LCs. Indeed, B. Zhang et al. (2006), J. A. Nousek et al. (2006), and B.-B. Zhang et al. (2007) explored Swift-XRT LCs and proposed energy injection as a potential scenario to account for the plateau phase or shallow decay phase in GRB afterglows (B. Zhang et al. 2006;

Table 6
Summary of Results of the CRs Obtained with Gamma-Ray Parameters (α_γ and β_γ) without Energy Injection ($q = 1$) and with Energy Injection ($q = 0$)

No Energy Injection ($q = 1$) in Gamma Rays								
$n(r)$	Cooling	ν Range	$\beta(p)$	CR:$1 < p < 2$	CR:$p > 2$	GRBs	Occurrence Rate	Figures
r^0	Slow/fast	$\nu > \max\{\nu_c, \nu_m\}$	$\frac{p}{2}$	$\frac{3\beta+5}{8}$	$\frac{3\beta-1}{2}$	3	21.4%	4(a)
r^{-1}	Slow/fast	$\nu > \max\{\nu_c, \nu_m\}$	$\frac{p}{2}$	$\frac{\beta+2}{3}$	$\frac{3\beta-1}{2}$	3	21.4%	4(b)
$r^{-1.5}$	Slow/fast	$\nu > \max\{\nu_c, \nu_m\}$	$\frac{p}{2}$	$\frac{3\beta+7}{10}$	$\frac{3\beta-1}{2}$	3	21.4%	4(c)
r^{-2}	Slow/fast	$\nu > \max\{\nu_c, \nu_m\}$	$\frac{p}{2}$	$\frac{\beta+3}{4}$	$\frac{3\beta-1}{2}$	3	21.4%	4(d)
$r^{-2.5}$	Slow/fast	$\nu > \max\{\nu_c, \nu_m\}$	$\frac{p}{2}$	$\frac{\beta+5}{6}$	$\frac{3\beta-1}{2}$	3	21.4%	4(e)

Energy Injection ($q = 0$) in Gamma Rays							
$n(r)$	Cooling	ν Range	$\beta(p)$	CR:$p > 2$	GRBs	Occurrence Rate	Figures
r^0	Slow/fast	$\nu > \max\{\nu_c, \nu_m\}$	$\frac{p}{2}$	$\beta - 1$	1	7.14%	4(f)
r^{-1}	Slow/fast	$\nu > \max\{\nu_c, \nu_m\}$	$\frac{p}{2}$	$\beta - 1$	1	7.14%	4(g)
$r^{-1.5}$	Slow/fast	$\nu > \max\{\nu_c, \nu_m\}$	$\frac{p}{2}$	$\beta - 1$	1	7.14%	4(h)
r^{-2}	Slow/fast	$\nu > \max\{\nu_c, \nu_m\}$	$\frac{p}{2}$	$\beta - 1$	1	7.14%	4(i)
$r^{-2.5}$	Slow/fast	$\nu > \max\{\nu_c, \nu_m\}$	$\frac{p}{2}$	$\beta - 1$	1	7.14%	4(j)

Note. Shows the number and occurrence rate of GRBs satisfying each relation between α and β (where α = is omitted for brevity) out of a total of 14 GRBs. Since each occurrence rate is calculated independently from the total sample of 14 GRBs, there is no obligation for the rates to add up to 100%.

Table 7
Summary of Results of the CRs Obtained with X-Ray Parameters (α_X and β_X) without Energy Injection ($q = 1$), with Energy Injection ($q = 0$), and with a Jet Break

No Energy Injection in X-Rays ($q = 1$)

$n(r)$	Cooling	ν Range	$\beta(p)$	CR:$1 < p < 2$	CR:$p > 2$	GRBs	Occurrence Rate	Figures
r^0	Slow	$\nu_m < \nu < \nu_c$	$\frac{p-1}{2}$	$\frac{6\beta+9}{16}$	$\frac{3\beta}{2}$	9	64.3%	5(a)
r^{-1}	Slow	$\nu_m < \nu < \nu_c$	$\frac{p-1}{2}$	$\frac{4\beta+9}{12}$	$\frac{9\beta+1}{6}$	8	57.1%	5(d)
$r^{-1.5}$	Slow	$\nu_m < \nu < \nu_c$	$\frac{p-1}{2}$	$\frac{3\beta+9}{10}$	$\frac{15\beta+3}{10}$	8	57.1%	5(g)
r^{-2}	Slow	$\nu_m < \nu < \nu_c$	$\frac{p-1}{2}$	$\frac{2\beta+9}{8}$	$\frac{3\beta+1}{2}$	5	35.7%	5(j)
$r^{-2.5}$	Slow	$\nu_m < \nu < \nu_c$	$\frac{p-1}{2}$	$\frac{\beta+9}{6}$	$\frac{9\beta+5}{6}$	1	7.14%	5(m)
r^0	Fast	$\nu_c < \nu < \nu_m$	$\frac{1}{2}$	$\frac{\beta}{2}$	$\frac{\beta}{2}$	0	0%	5(b)
r^{-1}	Fast	$\nu_c < \nu < \nu_m$	$\frac{1}{2}$	$\frac{\beta}{2}$	$\frac{\beta}{2}$	0	0%	5(e)
$r^{-1.5}$	Fast	$\nu_c < \nu < \nu_m$	$\frac{1}{2}$	$\frac{\beta}{2}$	$\frac{\beta}{2}$	0	0%	5(h)
r^{-2}	Fast	$\nu_c < \nu < \nu_m$	$\frac{1}{2}$	$\frac{\beta}{2}$	$\frac{\beta}{2}$	0	0%	5(k)
$r^{-2.5}$	Fast	$\nu_c < \nu < \nu_m$	$\frac{1}{2}$	$\frac{\beta}{2}$	$\frac{\beta}{2}$	0	0%	5(n)
r^0	Slow/fast	$\nu > \max\{\nu_c, \nu_m\}$	$\frac{p}{2}$	$\frac{3\beta+5}{8}$	$\frac{3\beta-1}{2}$	3	21.4%	5(c)
r^{-1}	Slow/fast	$\nu > \max\{\nu_c, \nu_m\}$	$\frac{p}{2}$	$\frac{\beta+2}{3}$	$\frac{3\beta-1}{2}$	3	21.4%	5(f)
$r^{-1.5}$	Slow/fast	$\nu > \max\{\nu_c, \nu_m\}$	$\frac{p}{2}$	$\frac{3\beta+7}{10}$	$\frac{3\beta-1}{2}$	3	21.4%	5(i)
r^{-2}	Slow/fast	$\nu > \max\{\nu_c, \nu_m\}$	$\frac{p}{2}$	$\frac{\beta+3}{4}$	$\frac{3\beta-1}{2}$	3	21.4%	5(l)
$r^{-2.5}$	Slow/fast	$\nu > \max\{\nu_c, \nu_m\}$	$\frac{p}{2}$	$\frac{\beta+5}{6}$	$\frac{3\beta-1}{2}$	3	21.4%	5(o)

Energy Injection in X-Rays ($q = 0$)

$n(r)$	Cooling	ν Range	$\beta(p)$	CR:$p > 2$	GRBs	Occurrence Rate	Figures
r^0	Slow	$\nu_m < \nu < \nu_c$	$\frac{p-1}{2}$	$\beta - 1$	0	0%	6(a)
r^{-1}	Slow	$\nu_m < \nu < \nu_c$	$\frac{p-1}{2}$	$\beta - \frac{2}{3}$	0	0%	6(d)
$r^{-1.5}$	Slow	$\nu_m < \nu < \nu_c$	$\frac{p-1}{2}$	$\beta - \frac{2}{5}$	1	7.14%	6(g)
r^{-2}	Slow	$\nu_m < \nu < \nu_c$	$\frac{p-1}{2}$	β	3	21.4%	6(j)
$r^{-2.5}$	Slow	$\nu_m < \nu < \nu_c$	$\frac{p-1}{2}$	$\frac{\beta+2}{3}$	3	21.4%	6(m)
r^0	Fast	$\nu_c < \nu < \nu_m$	$\frac{1}{2}$	$-\beta$	0	0%	6(b)
r^{-1}	Fast	$\nu_c < \nu < \nu_m$	$\frac{1}{2}$	$-\beta$	0	0%	6(e)
$r^{-1.5}$	Fast	$\nu_c < \nu < \nu_m$	$\frac{1}{2}$	$-\beta$	0	0%	6(h)
r^{-2}	Fast	$\nu_c < \nu < \nu_m$	$\frac{1}{2}$	$-\beta$	0	0%	6(k)
$r^{-2.5}$	Fast	$\nu_c < \nu < \nu_m$	$\frac{1}{2}$	$-\beta$	0	0%	6(n)
r^0	Slow/fast	$\nu > \max\{\nu_c, \nu_m\}$	$\frac{p}{2}$	$\beta - 1$	0	0%	6(c)
r^{-1}	Slow/fast	$\nu > \max\{\nu_c, \nu_m\}$	$\frac{p}{2}$	$\beta - 1$	0	0%	6(f)
$r^{-1.5}$	Slow/fast	$\nu > \max\{\nu_c, \nu_m\}$	$\frac{p}{2}$	$\beta - 1$	0	0%	6(i)
r^{-2}	Slow/fast	$\nu > \max\{\nu_c, \nu_m\}$	$\frac{p}{2}$	$\beta - 1$	0	0%	6(l)
$r^{-2.5}$	Slow/fast	$\nu > \max\{\nu_c, \nu_m\}$	$\frac{p}{2}$	$\beta - 1$	0	0%	6(o)

Jet Break in X-Rays						
Cooling	ν Range	$\beta(p)$	CR:$1 < p < 2$	GRBs	Occurrence Rate	Figures
Slow	$\nu_m < \nu < \nu_c$	$\frac{p-1}{2}$	$2\beta + 1$	0	0%	9(a)
Fast	$\nu_c < \nu < \nu_m$	1	$\frac{1}{2}$	0	0%	9(b)
Slow/fast	$\nu > \max\{\nu_c, \nu_m\}$	p	$\frac{\beta}{2}$	2	14.3%	9(c)

Note. Shows the number and occurrence rate of GRBs satisfying each relation (where $\alpha =$ is omitted for brevity) out of a total of 14 GRBs. Since each occurrence rate is calculated independently from the total sample of 14 GRBs, there is no obligation for the rates to add up to 100%.

Table 8
CRs Determined by Optical Parameters ($\alpha_{\rm opt}$ and $\beta_{\rm opt}$) without Energy Injection ($q = 1$), with Energy Injection ($q = 0$), and with a Jet Break

No Energy Injection ($q = 1$) in Optical

$n(r)$	Cooling	ν Range	$\beta(p)$	CR:$1 < p < 2$	CR:$p > 2$	GRBs	Occurrence Rate	Figures
r^0	Slow	$\nu_m < \nu < \nu_c$	$\frac{p-1}{2}$	$\frac{6\beta+9}{16}$	$\frac{3\beta}{2}$	0	0%	7(a)
r^{-1}	Slow	$\nu_m < \nu < \nu_c$	$\frac{p-1}{2}$	$\frac{4\beta+9}{12}$	$\frac{9\beta+1}{6}$	0	0%	7(d)
$r^{-1.5}$	Slow	$\nu_m < \nu < \nu_c$	$\frac{p-1}{2}$	$\frac{3\beta+9}{10}$	$\frac{15\beta+3}{10}$	0	0%	7(g)
r^{-2}	Slow	$\nu_m < \nu < \nu_c$	$\frac{p-1}{2}$	$\frac{2\beta+9}{8}$	$\frac{3\beta+1}{2}$	0	0%	7(j)
$r^{-2.5}$	Slow	$\nu_m < \nu < \nu_c$	$\frac{p-1}{2}$	$\frac{\beta+9}{6}$	$\frac{9\beta+5}{6}$	0	0%	7(m)
r^0	Fast	$\nu_c < \nu < \nu_m$	$\frac{1}{2}$	$\frac{\beta}{2}$	$\frac{\beta}{2}$	0	0%	7(b)
r^{-1}	Fast	$\nu_c < \nu < \nu_m$	$\frac{1}{2}$	$\frac{\beta}{2}$	$\frac{\beta}{2}$	0	0%	7(e)
$r^{-1.5}$	Fast	$\nu_c < \nu < \nu_m$	$\frac{1}{2}$	$\frac{\beta}{2}$	$\frac{\beta}{2}$	0	0%	7(h)
r^{-2}	Fast	$\nu_c < \nu < \nu_m$	$\frac{1}{2}$	$\frac{\beta}{2}$	$\frac{\beta}{2}$	0	0%	7(k)
$r^{-2.5}$	Fast	$\nu_c < \nu < \nu_m$	$\frac{1}{2}$	$\frac{\beta}{2}$	$\frac{\beta}{2}$	0	0%	7(n)
r^0	Slow/fast	$\nu > \max\{\nu_c, \nu_m\}$	$\frac{p}{2}$	$\frac{3\beta+5}{8}$	$\frac{3\beta-1}{2}$	2	14.3%	7(c)
r^{-1}	Slow/fast	$\nu > \max\{\nu_c, \nu_m\}$	$\frac{p}{2}$	$\frac{\beta+2}{3}$	$\frac{3\beta-1}{2}$	2	14.3%	7(f)
$r^{-1.5}$	Slow/fast	$\nu > \max\{\nu_c, \nu_m\}$	$\frac{p}{2}$	$\frac{3\beta+7}{10}$	$\frac{3\beta-1}{2}$	2	14.3%	7(i)
r^{-2}	Slow/fast	$\nu > \max\{\nu_c, \nu_m\}$	$\frac{p}{2}$	$\frac{\beta+3}{4}$	$\frac{3\beta-1}{2}$	2	14.3%	7(l)
$r^{-2.5}$	Slow/fast	$\nu > \max\{\nu_c, \nu_m\}$	$\frac{p}{2}$	$\frac{\beta+5}{6}$	$\frac{3\beta-1}{2}$	3	21.4%	7(o)

Energy Injection ($q = 0$) in Optical

$n(r)$	Cooling	ν Range	$\beta(p)$	CR:$p > 2$	GRBs	Occurrence Rate	Figures
r^0	Slow	$\nu_m < \nu < \nu_c$	$\frac{p-1}{2}$	$\beta - 1$	0	0%	8(a)
r^{-1}	Slow	$\nu_m < \nu < \nu_c$	$\frac{p-1}{2}$	$\beta - \frac{2}{3}$	1	7.14%	8(d)
$r^{-1.5}$	Slow	$\nu_m < \nu < \nu_c$	$\frac{p-1}{2}$	β	0	0%	8(g)
r^{-2}	Slow	$\nu_m < \nu < \nu_c$	$\frac{p-1}{2}$	$\beta - \frac{2}{5}$	1	7.14%	8(j)
$r^{-2.5}$	Slow	$\nu_m < \nu < \nu_c$	$\frac{p-1}{2}$	$\frac{\beta+2}{3}$	1	7.14%	8(m)
r^0	Fast	$\nu_c < \nu < \nu_m$	$\frac{1}{2}$	$-\beta$	0	0%	8(b)
r^{-1}	Fast	$\nu_c < \nu < \nu_m$	$\frac{1}{2}$	$-\beta$	0	0%	8(e)
$r^{-1.5}$	Fast	$\nu_c < \nu < \nu_m$	$\frac{1}{2}$	$-\beta$	0	0%	8(h)
r^{-2}	Fast	$\nu_c < \nu < \nu_m$	$\frac{1}{2}$	$-\beta$	0	0%	8(k)
$r^{-2.5}$	Fast	$\nu_c < \nu < \nu_m$	$\frac{1}{2}$	$-\beta$	0	0%	8(n)
r^0	Slow/fast	$\nu > \max\{\nu_c, \nu_m\}$	$\frac{p}{2}$	$\beta - 1$	0	0%	8(c)
r^{-1}	Slow/fast	$\nu > \max\{\nu_c, \nu_m\}$	$\frac{p}{2}$	$\beta - 1$	0	0%	8(f)
$r^{-1.5}$	Slow/fast	$\nu > \max\{\nu_c, \nu_m\}$	$\frac{p}{2}$	$\beta - 1$	0	0%	8(i)
r^{-2}	Slow/fast	$\nu > \max\{\nu_c, \nu_m\}$	$\frac{p}{2}$	$\beta - 1$	0	0%	8(l)
$r^{-2.5}$	Slow/fast	$\nu > \max\{\nu_c, \nu_m\}$	$\frac{p}{2}$	$\beta - 1$	0	0%	8(o)

Jet Break in Optical						
Cooling	ν Range	$\beta(p)$	CR:$1 < p < 2$	GRBs	Occurrence Rate	Figures
Slow	$\nu_m < \nu < \nu_c$	$\frac{p-1}{2}$	$2\beta + 1$	0	0%	9(d)
Fast	$\nu_c < \nu < \nu_m$	1	$\frac{1}{2}$	0	0%	9(e)
Slow/fast	$\nu > \max\{\nu_c, \nu_m\}$	p	$\frac{\beta}{2}$	0	0%	9(f)

Note. Shows the number and occurrence rate of GRBs satisfying each relation (where $\alpha =$ is omitted for brevity) out of a total of 14 GRBs. Since each occurrence rate is calculated independently from the total sample of 14 GRBs, there is no obligation for the rates to add up to 100%.

Table 9
Summary of the Fulfillment of CRs in Multiple Wavelengths for the No-energy-injection and Energy-injection Scenarios

GRB Name	Wavelengths	$k=0$			$k=1$			$k=1.5$			$k=2$			$k=2.5$			Preferred Medium
		SC	FC	SC/FC	SC	FC	SC/FC	SC	FC	SC/FC	SC	FC	SC/FC	SC	FC	SC/FC	
No Energy Injection ($q=1$)																	
090328A	X	X	⋯	⋯	X	⋯	⋯	X	⋯	⋯	X	⋯	⋯	⋯	⋯	⋯	$k=0$, 1, 1.5, 2
090510A	X	⋯	⋯	⋯	⋯	⋯	⋯	⋯	⋯	⋯	X	⋯	⋯	X	⋯	⋯	$k=2$, 2.5
090902B	X, O	⋯	⋯	O	X	⋯	O	X	⋯	O	⋯	⋯	O	⋯	⋯	O	All
090926A	γ, X	X	⋯	γ	⋯	⋯	γ	⋯	⋯	γ	⋯	⋯	γ	⋯	⋯	γ	All
120711A	X	⋯	⋯	⋯	⋯	⋯	⋯	X	⋯	⋯	⋯	⋯	⋯	⋯	⋯	⋯	$k=1.5$
130427A	X, O	X	⋯	O	X	⋯	O	X	⋯	O	⋯	⋯	O	⋯	⋯	O	All
141028A	X	X	⋯	X	⋯	⋯	X	⋯	⋯	X	⋯	⋯	X	⋯	⋯	X	All
160625B	X	X	⋯	X	X	⋯	X	X	⋯	X	X	⋯	X	⋯	⋯	X	All
170405A	X, O	X	⋯	X	X	⋯	X	X	⋯	X	X	⋯	X	⋯	⋯	X, O	All
171010A	γ, X	X	⋯	γ	X	⋯	γ	⋯	⋯	γ	⋯	⋯	γ	⋯	⋯	γ	All
180720B	X	X	⋯	⋯	⋯	⋯	⋯	⋯	⋯	⋯	⋯	⋯	⋯	⋯	⋯	⋯	$k=0$
210822A	X	⋯	⋯	⋯	⋯	⋯	⋯	⋯	⋯	⋯	X	⋯	⋯	⋯	⋯	⋯	$k=2$
220101A	X	⋯	⋯	⋯	X	⋯	⋯	X	⋯	⋯	⋯	⋯	⋯	⋯	⋯	⋯	$k=1$, 1.5
230812B	γ, X	X	⋯	γ	X	⋯	γ	X	⋯	γ	⋯	⋯	γ	⋯	⋯	γ	All
Energy Injection ($q=0$)																	
090328A	X, O	⋯	⋯	⋯	⋯	⋯	⋯	⋯	⋯	⋯	O	⋯	⋯	X	⋯	⋯	$k=2$, 2.5
090510A	X	⋯	⋯	⋯	⋯	⋯	⋯	⋯	⋯	⋯	X	⋯	⋯	⋯	⋯	⋯	$k=2$
090902B	X	⋯	⋯	⋯	⋯	⋯	⋯	⋯	⋯	⋯	⋯	⋯	⋯	X	⋯	⋯	$k=2.5$
090926A	O	⋯	⋯	⋯	O	⋯	⋯	⋯	⋯	⋯	⋯	⋯	⋯	⋯	⋯	⋯	$k=1$
120711A	⋯	⋯	⋯	⋯	⋯	⋯	⋯	⋯	⋯	⋯	⋯	⋯	⋯	⋯	⋯	⋯	None
130427A	⋯	⋯	⋯	⋯	⋯	⋯	⋯	⋯	⋯	⋯	⋯	⋯	⋯	⋯	⋯	⋯	None
141028A	X	⋯	⋯	⋯	⋯	⋯	⋯	X	⋯	⋯	X	⋯	⋯	⋯	⋯	⋯	$k=1.5$, 2
160625B	⋯	⋯	⋯	⋯	⋯	⋯	⋯	⋯	⋯	⋯	⋯	⋯	⋯	⋯	⋯	⋯	None
170405A	X, O	⋯	⋯	⋯	⋯	⋯	⋯	⋯	⋯	⋯	X	⋯	⋯		⋯	⋯	$k=2$, 2.5
171010A	⋯	⋯	⋯	⋯	⋯	⋯	⋯	⋯	⋯	⋯	⋯	⋯	⋯	⋯	⋯	⋯	None
180720B	⋯	⋯	⋯	⋯	⋯	⋯	⋯	⋯	⋯	⋯	⋯	⋯	⋯	⋯	⋯	⋯	None
210822A	⋯	⋯	⋯	⋯	⋯	⋯	⋯	⋯	⋯	⋯	⋯	⋯	⋯	⋯	⋯	⋯	None
220101A	γ	⋯	⋯	γ	⋯	⋯	γ	⋯	⋯	γ	⋯	⋯	γ	⋯	⋯	γ	All
230812B	X	⋯	⋯	⋯	⋯	⋯	⋯	⋯	⋯	⋯	⋯	⋯	⋯	X	⋯	⋯	$k=2$

Note. Column (1): GRB names. Column (2): corresponding wavelengths for which a GRB fulfills a given CR: "γ" for gamma rays, "X" for X-rays, and "O" for optical. Columns (3)–(7): the fulfillment status of the given CR in the environment of the SC, FC, and SC/FC regimes for $k=0$ (ISM), $k=2$ (stellar wind environment), and $k=1$, 1.5, 2.5 (stratified medium) for each GRB. Column (8): the preferred medium for each GRB.

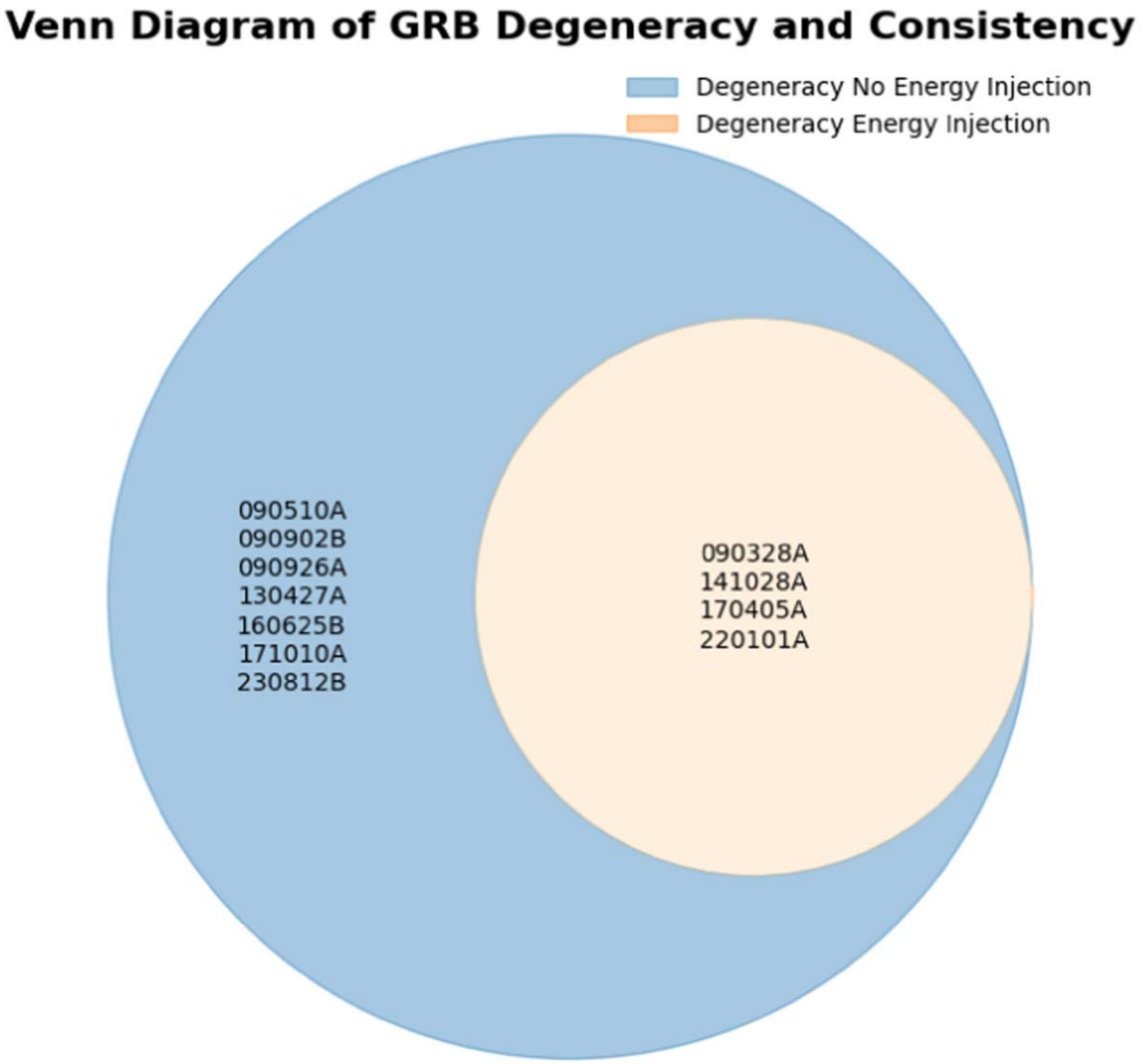

Figure 11. Venn diagram representing the degeneracy compared to the k values among the 14 GRBs in the scenarios both with and without energy injection. The color-coding represents the two regimes, with energy injection in orange and no energy injection in blue.

J. A. Nousek et al. 2006). However, M. Ackermann et al. (2013) examined GRB 110731A using multiwavelength observations and indicated that the afterglows of some Fermi-LAT GRBs are dominated by bright FS emission rather than a prolonged episode of energy injection. Furthermore, as discussed in Section 1.1, D. Tak et al. (2019) found that 48 out of 59 GRBs observed by Fermi-LAT satisfied at least one CR, thus showing that the standard fireball model is able to explain most of the observations. D. Tak et al. (2019) show that the preferred density is a constant-density medium, while in our case both the constant density and stellar wind are almost equally probable for the no-energy-injection scenario. However, the difference between D. Tak et al. (2019) and our study is that, in our study, we use a deterministic approach with stratified stellar wind, with several values of k, while in D. Tak et al. (2019) a probabilistic approach is taken and only a constant-density medium and a wind medium were investigated. Indeed, M. G. Dainotti et al. (2021b) reinforces our results again, as they also found that most of their Fermi-LAT GRBs adhere to the CRs for the no-energy-injection scenario. These studies and our study strongly suggest that the no-energy-injection scenario is sufficient to explain the dynamics of a significant portion of GRB afterglows in the high-energy regime. This conclusion poses challenges to the previously accepted paradigm of invoking the energy-injection scenario. It highlights the reliability of the standard fireball model in explaining GRB afterglows without invoking continuous energy injection for many LAT-detected bursts.

When comparing the seven GRBs (090328A, 090902B, 090926A, 120711A, 130427A, 141028A, and 160625B) common to both our study and the analysis conducted by B. P. Gompertz et al. (2018), we observed some discrepancies in the preferred environments, as outlined in Table 10. There are two notable cases that have a defined medium in our study: 120711A, with $k = 1.5$ in the no-energy-injection scenario, and GRB 090926A, with $k = 1$ in the energy-injection scenario, while B. P. Gompertz et al. (2018) both have a wind medium. However, one has to note that the case of GRB 120711 is more controversial, since in the energy-injection scenario none of the k values can be determined. On the other hand, GRB 090926A in the no-energy-injection scenario has a degeneracy since all values of k are possible and, therefore, also a wind medium. Another notable case, undetermined by B. P. Gompertz et al. (2018), is GRB 141028A, where we find that $k = 1.5$ and 2 are

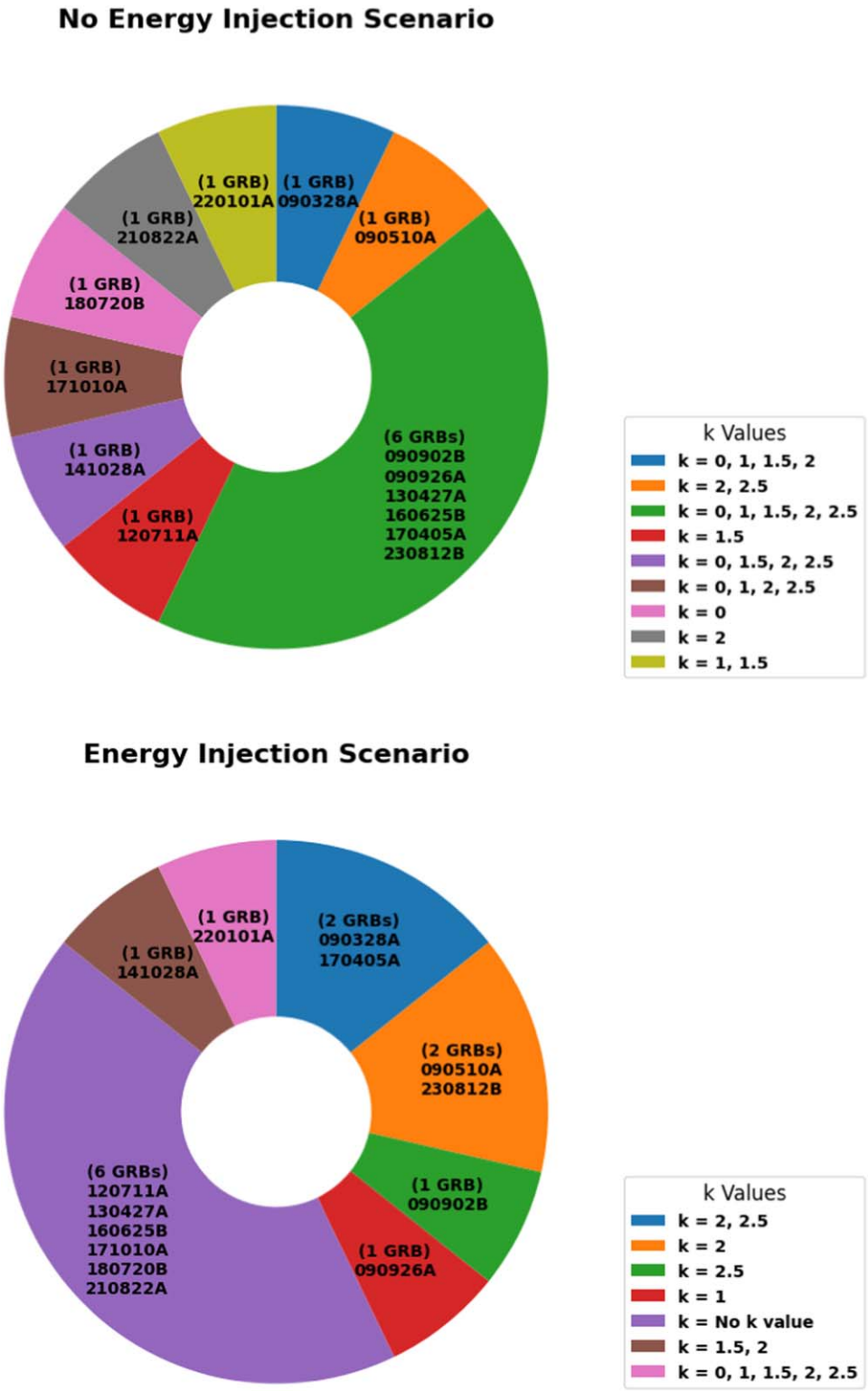

Figure 12. Pie chart representing the environment determination for each of the GRBs. The color-coding indicates different k values or different combinations of those values, as reported in the legend on the right. The upper and lower panels show the cases of no energy and energy injection, respectively.

viable for the energy-injection scenario, and additionally $k = 0$ and 2.5 are possible for the no-energy-injection case. Given the degeneracies within the same GRBs, it is often challenging to draw a definite conclusion on the environments. The key difference between B. P. Gompertz et al. (2018) and our study is that they estimated the best-fit value of the electron distribution PL index, p, by calculating a weighted mean of the p values, including the error bars which were determined using both the α and β indices from X-ray and optical data. They analyzed five different scenarios based on the relative positions of the following frequencies: cooling, ν_c, the X-ray, ν_x, and optical in the R band, ν_R. These scenarios included the following: $\nu_c < \nu_R < \nu_x$, $\nu_R < \nu_c < \nu_x$, and $\nu_R < \nu_x < \nu_c$ in an ISM environment, and $\nu_R < \nu_c < \nu_x$ and $\nu_R < \nu_x < \nu_c$ in a wind

Table 10
Comparison of the Preferred Environment of Seven GRBs Common between Our Study and the Analysis of B. P. Gompertz et al. (2018)

Comparison of Preferred Environment with B. P. Gompertz et al. (2018)			
GRB Name	B. P. Gompertz et al. (2018)	Our Study No Energy Injection ($q = 1$)	Our Study Energy Injection ($q = 0$)
090328A	$k = 0$	$k = 0$, 1, 1.5, 2	$k = 2$, 2.5
090902B	$k = 0$	$k = 0$, 1, 1.5, 2, 2.5	$k = 2.5$
090926A	$k = 2$	$k = 0$, 1, 1.5, 2, 2.5	$k = 1$
120711A	$k = 2$	$k = 1.5$	None
130427A	$k = 2$	$k = 0$, 1, 1.5, 2, 2.5	None
141028A	Unknown	$k = 0$, 1, 1.5, 2, 2.5	$k = 1.5$, 2
160625B	$k = 0$	$k = 0$, 1, 1.5, 2, 2.5	None

environment. Instead of computing the p values, we directly fit the CRs using the observed α and β values from gamma-ray, X-ray, and optical data for both energy and no energy injection. However, in our case, we also have a detailed method for computing the error bars by defining ellipses regions (see Section 4). A key difference is that we also explored a stratified medium ($k = 1$, 1.5, and 2.5) along with the wind ($k = 2$) and ISM ($k = 0$) cases, while they focused on $k = 0$ and 2. Another difference in the preferred environments between our study and their analysis resides in the LC fitting. B. P. Gompertz et al. (2018) relied on the automated LC fits available in the Swift-XRT catalog for X-ray data. For the optical data, they primarily used values from existing literature when available and, in cases where they were not, fitted the LCs using data from GCN circulars, applying either a PL or BPL model. In contrast, we fit both X-ray and optical LCs following the GRBLC package (M. G. Dainotti et al. 2024) with either a PL or BPL, or their combinations, as appropriate. Additionally, we performed a homogeneous analysis of the optical data (see Section 3).

As a matter of fact, given that our optical LCs have been processed separately in a uniform way by adding all the available data in the literature, including GCN and private communication, has guaranteed a more uniform treatment of the sample, also in view of the color evolution analysis. Continuing on the comparison between the optical and X-ray data analyzed together, it is worth mentioning the treatment by X.-G. Wang et al. (2015), as we have mentioned in Section 4.2, where 85 GRBs with simultaneous observations in optical and X-rays were discussed. The treatment of X.-G. Wang et al. (2015) is analytical in nature, similar to our approach. Also, the general conclusion about the reliability of the standard FS model is similar since at least half of the GRBs in the sample can be explained within the simple afterglow FS model, but there are some cases, segments in the LCs in which the CRs are not fulfilled, and three out of 85 cases in which none of the CRs is satisfied. The conclusion of X.-G. Wang et al. (2015) is that one can indeed recover more cases following the standard model if one also includes the long-lasting RS, structured jets, and stratified circumburst medium density profile with values of k other than 0 and 2. Indeed, this is similar to what we recovered in our study since the number of cases following the CRs is characterized by a stratified medium that includes $k = 1$, 1.5, and 2.5.

In the X-ray data, in this current analysis without energy injection, the SC ($\nu_m < \nu < \nu_c$) regime with a constant-density medium (with $k = 0$ there are nine cases of fulfillment) emerges as the most favored, followed by a stratified medium for $k = 1$ and 1.5 with eight cases.

Also, G. P. Srinivasaragavan et al. (2020) under a case with no energy injection showed a disagreement between CRs at high and low energies, suggesting that the emission mechanism may differ at high energies for those without energy injection. It is worth noting that in both the no-energy-injection and energy-injection scenarios, none of the GRBs in our sample demonstrates a preference for the FC ($\nu_c < \nu < \nu_m$) regime for any value of k in either X-rays or the optical band. In scenarios involving energy injection, our investigation highlights that the SC ($\nu_m < \nu < \nu_c$) regime across X-ray and optical wavelengths (seven GRBs: GRB 090328A, 090510A, 090902B, 090926A, 141028A, 170405A, and 230812B) is the most preferred versus the other regimes; for example, the SC/FC regime has no case fulfilled. Here, we also note that in another study, conducted by M. G. Dainotti et al. (2021a) in the X-ray, the SC ($\nu_m < \nu < \nu_c$) regime was found to be the preferred regime within the context of energy injection. The FC ($\nu_c < \nu < \nu_m$) regime remains the least favored regime, with none of the examined GRBs satisfying it across X-ray and optical wavelengths for any k value.

6. Summary and Conclusions

We tested the external FS model through a set of CRs with a sample of 14 GRBs observed contemporaneously in gamma-ray, X-ray, and optical bands by various space-based and ground-based telescopes. We observe that most of our sample satisfies at least one CR, indicating that the external FS model can explain numerous characteristics observed in GRBs. If a GRB satisfies multiple CRs, it indicates the existence of equally plausible scenarios, indicating a more complex nature of the GRB mechanism. It is crucial to acknowledge that in numerous instances there is a degeneracy of scenarios. However, our results remain significant since they enable us to exclude certain scenarios. The inclusion of multiple wavelengths provides an opportunity to break these degeneracies. If we wish to reconduct this study adapted to a constant or wind medium, we can assess that, in the no-energy-injection scenario, the number of GRBs with $k = 0$ is 10, while the number of GRBs with $k = 2$ is 11. In the energy-injection scenario, we have one case only for $k = 0$, and six cases with $k = 2$. B. P. Gompertz et al. (2018) have discussed the equal split and how this relates to the progenitor. Almost equality may arise from two options: a diverse progenitor, or the same progenitor but with a different environment relating to a

different evolutionary stage. One could imagine that a star with a weak stellar wind in its final stage will influence the environment less than a star characterized by a strong wind type. Simplistically, one can assume that more massive stars emit more energy and radiate a strong stellar wind. However, this hypothesis, which was tested via a Kolmogorov–Smirnov test, does not yield a significant difference between the cumulative distribution of the GRBs characterized by the wind and the constant medium. The interesting perspective discussed in B. P. Gompertz et al. (2018) is that there is room for fitting a medium with $k = 1$ with some GRBs. Indeed, this is what we did by expanding the stratified medium to different values of k. Hence, it is still worth enlarging the sample and investigating this issue more in the future.

Another takeaway of this study is that the degeneracy we found is challenging to break, and the stratified medium scenario can occur when the emission is unstable. Still, another possibility to look at this scenario and to attempt to break this degeneracy is to take one step back and consider only the two possibilities of wind and constant medium but enlarge the cases with different values of the q parameter (e.g., -0.5, -0.3, 0.3, and 0.5). This analysis will be the object of a forthcoming paper.

Acknowledgments

We thank the work of Rishav Bhattacharjee for his help in developing the initial code for showing the multiwavelength LCs. We are particularly grateful to Prof. Bing Zhang for the very useful comments about the conclusion on the stratified medium versus the constant medium and the problem of the degeneration of the parameters. E.B. is grateful to NAOJ for hosting her at the Comos Lodge in 2023 June, where the collaboration on this paper started. E.B. is also grateful to the Project Title: H2020-MSCA-RISE-2016 NEWS, Project ID Number: 734303 for supporting her visit to NAOJ.

ORCID iDs

M. G. Dainotti https://orcid.org/0000-0003-4442-8546
S. Bhardwaj https://orcid.org/0000-0003-4709-0915
E. Bissaldi https://orcid.org/0000-0001-9935-8106
N. Fraija https://orcid.org/0000-0002-0173-6453
S. Sourav https://orcid.org/0000-0002-0169-4003
A. Galvan-Gamez https://orcid.org/0000-0001-5193-3693

References

Ackermann, M., Ajello, M., Asano, K., et al. 2013, ApJ, 763, 71
Ackermann, M., Ajello, M., Baldini, L., et al. 2013, ApJ, 763, 71
Ackermann, M., Asano, K., Atwood, W. B., et al. 2010, ApJ, 716, 1178
Afonso, P., Greiner, J., Pian, E., et al. 2011, A&A, 526, A154
Ajello, M., Arimoto, M., Axelsson, M., et al. 2019, ApJ, 878, 52
Akaike, H. 1974, ITAC, 19, 716
Angulo-Valdez, C., Becerra, R. L., Pereyra, M., et al. 2024, MNRAS, 527, 8140
Atwood, W. B., Abdo, A. A., Ackermann, M., et al. 2009, ApJ, 697, 1071
Beniamini, P., Giannios, D., & Metzger, B. D. 2017, MNRAS, 472, 3058
Beniamini, P., & Mochkovitch, R. 2017, A&A, 605, A60
Blandford, R. D., & McKee, C. F. 1976, PhFl, 19, 1130
Burgess, J. M., Bégué, D., Ryde, F., et al. 2016, ApJ, 822, 63
Cannizzo, J. K., & Gehrels, N. 2009, ApJ, 700, 1047
Cannizzo, J. K., Troja, E., & Gehrels, N. 2011, ApJ, 734, 35
Chevalier, R. A., & Li, Z. 2000, ApJ, 536, 195
Crowther, P. A. 2007, ARA&A, 45, 177
Dai, Z. G., & Lu, T. 1998, A&A, 333, L87
Dainotti, M., Levine, D., Fraija, N., et al. 2023, Galax, 11, 25
Dainotti, M., Petrosian, V., Willingale, R., et al. 2015, MNRAS, 451, 3898
Dainotti, M. G., Cardone, V. F., & Capozziello, S. 2008, MNRAS, 391, L79
Dainotti, M. G., De Simone, B., Malik, R. F. M., et al. 2024, MNRAS, 533, 4023
Dainotti, M. G., Hernandez, X., Postnikov, S., et al. 2017a, ApJ, 848, 88
Dainotti, M. G., Lenart, A. Ł., Fraija, N., et al. 2021a, PASJ, 73, 970
Dainotti, M. G., Lenart, A. Ł., Sarracino, G., et al. 2020a, ApJ, 904, 97
Dainotti, M. G., Levine, D., Fraija, N., Warren, D., & Sourav, S. 2022a, ApJ, 940, 169
Dainotti, M. G., Livermore, S., Kann, D. A., et al. 2020b, ApJL, 905, L26
Dainotti, M. G., Nagataki, S., Maeda, K., Postnikov, S., & Pian, E. 2017b, A&A, 600, A98
Dainotti, M. G., Nielson, V., Sarracino, G., et al. 2022b, MNRAS, 514, 1828
Dainotti, M. G., Omodei, N., Srinivasaragavan, G. P., et al. 2021b, ApJS, 255, 13
Dainotti, M. G., Ostrowski, M., & Willingale, R. 2011, MNRAS, 418, 2202
Dainotti, M. G., Petrosian, V., Singal, J., & Ostrowski, M. 2013, ApJ, 774, 157
Dainotti, M. G., Postnikov, S., Hernandez, X., & Ostrowski, M. 2016, ApJL, 825, L20
Dainotti, M. G., Willingale, R., Capozziello, S., Fabrizio Cardone, V., & Ostrowski, M. 2010, ApJL, 722, L215
Dainotti, M. G., Young, S., Li, L., et al. 2022c, ApJS, 261, 25
Dall'Osso, S., Stratta, G., Guetta, D., et al. 2011, A&A, 526, A121
De Colle, F., Granot, J., López-Cámara, D., & Ramirez-Ruiz, E. 2012a, ApJ, 746, 122
De Colle, F., Ramirez-Ruiz, E., Granot, J., & Lopez-Camara, D. 2012b, ApJ, 751, 57
Del Vecchio, R., Dainotti, M. G., & Ostrowski, M. 2016, ApJ, 828, 36
Dereli-Begue, H., Per, A., Ryde, F., et al. 2022, NatCo, 13, 5611
Evans, P. A., Beardmore, A. P., Page, K. L., et al. 2009, MNRAS, 397, 1177
Fraija, N., Betancourt Kamenetskaia, B., Galván-Gámez, A., et al. 2024a, MNRAS, 527, 1674
Fraija, N., Dainotti, M. G., Betancourt Kamenetskaia, B., Galván-Gámez, A., & Aguilar-Ruiz, E. 2024b, MNRAS, 527, 1884
Fraija, N., Dainotti, M. G., Kamenetskaia, B. B., Levine, D., & Galvan-Gamez, A. 2023a, MNRAS, 525, 1630
Fraija, N., Dainotti, M. G., Levine, D., Kamenetskaia, B. B., & Galvan-Gamez, A. 2023b, ApJ, 958, 126
Fraija, N., Dainotti, M. G., Ugale, S., Jyoti, D., & Warren, D. C. 2022a, ApJ, 934, 188
Fraija, N., De Colle, F., Veres, P., et al. 2020a, ApJ, 896, 25
Fraija, N., Dichiara, S., Pedreira, A. C. C. d. E. S., et al. 2019, ApJ, 885, 29
Fraija, N., Galvan-Gamez, A., Betancourt Kamenetskaia, B., et al. 2022b, ApJ, 940, 189
Fraija, N., Laskar, T., Dichiara, S., et al. 2020b, ApJ, 905, 112
Fraija, N., Veres, P., Beniamini, P., et al. 2021, ApJ, 918, 12
Frederiks, D., Golenetskii, S., Lysenko, A., et al. 2021, GCN, 30694, 1
Fukushima, T., To, S., Asano, K., & Fujita, Y. 2017, ApJ, 844, 92
Gao, H., Lei, W.-H., Zou, Y.-C., Wu, X.-F., & Zhang, B. 2013, NewAR, 57, 141
Gompertz, B. P., Fruchter, A. S., & Pe'er, A. 2018, arXiv:1802.07730
Gompertz, B. P., Fruchter, A. S., & Pe'er, A. 2018, ApJ, 866, 162
Gompertz, B. P., O'Brien, P. T., & Wynn, G. A. 2014, MNRAS, 438, 240
Gompertz, B. P., O'Brien, P. T., Wynn, G. A., & Rowlinson, A. 2013, MNRAS, 431, 1745
Gompertz, B. P., van der Horst, A. J., O'Brien, P. T., Wynn, G. A., & Wiersema, K. 2015, MNRAS, 448, 629
Granot, J., & Sari, R. 2002, ApJ, 568, 820
Hotokezaka, K., Kyutoku, K., Tanaka, M., et al. 2013, ApJL, 778, L16
Hussenot-Desenonges, T., Wouters, T., Guessoum, N., et al. 2024, MNRAS, 530, 1
Jelínek, M., Topinka, M., Karpov, S., et al. 2022, A&A, 662, A126
Jin, Z.-P., Zhou, H., Wang, Y., et al. 2023, arXiv:2301.02407
Kangas, T., & Fruchter, A. S. 2021, ApJ, 911, 14
Kangas, T., Fruchter, A. S., Cenko, S. B., et al. 2020, ApJ, 894, 43
Kouveliotou, C., Meegan, C. A., Fishman, G. J., et al. 1993, ApJL, 413, L101
Kumar, P., & Duran, R. B. 2009, MNRAS, 400, L75
Kumar, P., & Duran, R. B. 2010, MNRAS, 409, 226
Kumar, P., Narayan, R., & Johnson, J. L. 2008, Sci, 321, 376
Kumar, P., & Piran, T. 2000, ApJ, 532, 286
Kumar, P., & Zhang, B. 2015, PhR, 561, 1
Levine, D., Dainotti, M., Zvonarek, K. J., et al. 2022, ApJ, 925, 15
Li, L., Liang, E.-W., Tang, Q.-W., et al. 2012, ApJ, 758, 27
Li, L., Wang, Y., Shao, L., et al. 2018a, ApJS, 234, 26

Li, L., Wu, X.-F., Lei, W.-H., et al. 2018b, ApJS, 236, 26
Liang, E.-W., Racusin, J. L., Zhang, B., Zhang, B.-B., & Burrows, D. N. 2008, ApJ, 675, 528
Liang, E.-W., Zhang, B.-B., & Zhang, B. 2007, ApJ, 670, 565
Lien, A. Y., Barthelmy, S. D., Krimm, H. A., et al. 2021, GCN, 30689, 1
Lü, H.-J., & Zhang, B. 2014, ApJ, 785, 74
Lü, H.-J., Zhang, B., Lei, W.-H., Li, Y., & Lasky, P. D. 2015, ApJ, 805, 89
Melandri, A., Malesani, D. B., Izzo, L., et al. 2019, MNRAS, 490, 5366
Metzger, B. D., Beniamini, P., & Giannios, D. 2018, ApJ, 857, 95
Misra, K., Resmi, L., Kann, D. A., et al. 2021, MNRAS, 504, 5685
Nousek, J. A., Kouveliotou, C., Grupe, D., et al. 2006, ApJ, 642, 389
O'Brien, P. T., Willingale, R., Osborne, J., et al. 2006, ApJ, 647, 1213
Oates, S. R., Page, M. J., De Pasquale, M., et al. 2012, MNRAS, 426, L86
Panaitescu, A. 2011, MNRAS, 414, 1379
Panaitescu, A., & Kumar, P. 2000, ApJ, 543, 66
Racusin, J. L., Liang, E. W., Burrows, D. N., et al. 2009, ApJ, 698, 43
Ramirez-Ruiz, E., Dray, L. M., Madau, P., & Tout, C. A. 2001, MNRAS, 327, 829
Ramirez-Ruiz, E., García-Segura, G., Salmonson, J. D., & Pérez-Rendón, B. 2005, ApJ, 631, 435
Rea, N., Gullón, M., Pons, J. A., et al. 2015, ApJ, 813, 92
Rees, M. J., & Mészáros, P. 1998, ApJL, 496, L1
Rhoads, J. E. 1999, ApJ, 525, 737
Roming, P. W. A., Kennedy, T. E., Mason, K. O., et al. 2005, SSRv, 120, 95
Rowlinson, A., Gompertz, B. P., Dainotti, M., et al. 2014, MNRAS, 443, 1779
Rowlinson, A., O'Brien, P. T., Metzger, B. D., Tanvir, N. R., & Levan, A. J. 2013, MNRAS, 430, 1061
Rowlinson, A., O'Brien, P. T., Tanvir, N. R., et al. 2010, MNRAS, 409, 531
Ryan, G., van Eerten, H., Piro, L., & Troja, E. 2020, ApJ, 896, 166
Sakamoto, T., Hill, J. E., Yamazaki, R., et al. 2007, ApJ, 669, 1115
Sari, R., & Mészáros, P. 2000, ApJL, 535, L33
Sari, R., Narayan, R., & Piran, T. 1996, ApJ, 473, 204
Sari, R., & Piran, T. 1995, ApJL, 455, L143
Sari, R., & Piran, T. 1999, A&AS, 138, 537
Sari, R., Piran, T., & Halpern, J. P. 1999, ApJL, 519, L17
Sari, R., Piran, T., & Narayan, R. 1998, ApJL, 497, L17
Srinivasaragavan, G. P., Dainotti, M. G., Fraija, N., et al. 2020, ApJ, 903, 18
Srinivasaragavan, G. P., Swain, V., O'Connor, B., et al. 2024, ApJL, 960, L18
Stratta, G., Dainotti, M. G., Dall'Osso, S., Hernandez, X., & De Cesare, G. 2018, ApJ, 869, 155
Tagliaferri, G., Goad, M., Chincarini, G., et al. 2005, Natur, 436, 985
Tak, D., Omodei, N., Uhm, Z. L., et al. 2019, ApJ, 883, 134
Toma, K., Ioka, K., Sakamoto, T., & Nakamura, T. 2007, ApJ, 659, 1420
Troja, E., Cusumano, G., O'Brien, P. T., et al. 2007, ApJ, 665, 599
Tsvetkova, A., Frederiks, D., Lysenko, A., et al. 2022, GCN, 31433, 1
Veres, P., & Mészáros, P. 2014, ApJ, 787, 168
Wang, X.-G., Zhang, B., Liang, E.-W., et al. 2015, ApJS, 219, 9
Warren, D. C., Dainotti, M., Barkov, M. V., et al. 2022, ApJ, 924, 40
Yi, S.-X., Wu, X.-F., & Dai, Z.-G. 2013, ApJ, 776, 120
Yi, S.-X., Wu, X.-F., Zou, Y.-C., & Dai, Z.-G. 2020, ApJ, 895, 94
Zhang, B. 2007a, ChJAA, 7, 1
Zhang, B. 2011, CRPhy, 12, 206
Zhang, B. 2018, The Physics of Gamma-Ray Bursts (Cambridge: Cambridge Univ. Press)
Zhang, B., Fan, Y. Z., Dyks, J., et al. 2006, ApJ, 642, 354
Zhang, B., Liang, E., Page, K. L., et al. 2007a, ApJ, 655, 989
Zhang, B., & Mészáros, P. 2001, ApJL, 552, L35
Zhang, B., & Mészáros, P. 2004, IJMPA, 19, 2385
Zhang, B., Zhang, B.-B., Liang, E.-W., et al. 2007b, ApJL, 655, L25
Zhang, B.-B., Liang, E.-W., & Zhang, B. 2007, ApJ, 666, 1002
Zhang, B. 2014, IJMPD, 23, 1430002
Zhao, L., Zhang, B., Gao, H., et al. 2019, ApJ, 883, 97